UNIVERSITAT AUTÒNOMA DE BARCELONA

Departament de Física

Investigation of thermal bremsstrahlung emission from hot and fragmenting nuclear matter formed in ^{129}Xe + ^{nat}Sn reactions at $50A$ MeV

Raquel Ortega Comino
PhD Thesis

June 2003

Acknowledgments

There are many people I would like to thank for a huge variety of reasons. I am grateful to Yves Schutz, Ginés Martínez at SUBATECH and Francisco Fernández at the Universitat Autònoma de Barcelona for giving me the opportunity to work with their groups.

I am particularly grateful to Ginés Martínez, the spokesperson of the experiment and my advisor at SUBATECH. His knowlegment, insightful feedback and support have been of great importance and influence to me, both academically and personally. I'm also in debt with David d'Enterria, who initiated me into the TAPS physics and since then he has always been available to solve my doubts. I would also like to thank the rest of the (ex)members of the group photon at SUBATECH: Laurent Aphecetche and María Mora. I would like to thank Hughes Delagrange, who read the whole manuscript thoroughly and correct the English spelling and grammar and contributed also to the scientific discussion.

I want to thank all the members of my thesis comitee: Carme Baixeras, Herbert Loehner, Jack Martino, Artur Polls and Jean-Claude Steckmeyer, for accepting reading and commenting the thesis.

I want to express my gratitude to all the members of the TAPS Collaboration and to all the people that participated in the experiment, as well as Daniel Guerreau, the director of the GANIL laboratory.

I have been fortunate to interact with many people in Nantes and in Barcelona who have influenced me greatly. Many thanks to the colleagues who were resposinble of creating a pleaseant working and enjoying environment during my state at SUBATECH, Linda, Ludo, Fabrice, Javier, Tacklit... To my colleagues of the Grup de Física de les Radiacions in Barcelona: Khalil, Moaad for their patience and availability to solve my "logistic" problems through all of these years, Lluis, Tayeb, Andreu, Arnau, Raul... I would also like to thank my family and friends for the support they provide me, no matter where I am.

Contents

Chapter 1

Introduction

One of the challenges of modern nuclear physics is the identification of the different phases in which nuclear matter exists in the Universe or is expected to have been by theoretical predictions. On Earth all atomic nuclei are found in the ground state, defined by the saturation density, $\rho_0 = 0.17$ fm^{-3}, at zero pressure and temperature. At the present moment, the equation of state of nuclear matter (EoS), which describes the density and temperature dependence of the energy per nucleon, is only empirically determined at this state.

On the basis of the similarity between the Van der Waals and nucleon-nucleon interactions, with a long range attractive potential and a short range repulsive core, nuclei can be viewed as droplets of a Fermi liquid of protons and neutrons. At densities lower than ρ_0 and temperatures of a few MeV, this "nuclear liquid" is expected to undergo a first order phase transition to a gaseous state [1, 2]. Thus, as macroscopic liquids, infinite nuclear matter would exhibit a latent heat, corresponding to the breaking of bounds between nucleons, and a liquid-gas mixed phase in equilibrium at temperatures up to a critical temperature of $T_c \approx 10$ MeV. The liquid-gas phase transition plays an important role in the explosion of supernovae [3, 4]. For higher temperatures up to around 100 MeV nuclear matter is in the form of an hadron gas (Fig. 1.1). At temperatures in excess of $T_c^{QCD} \approx 170$ MeV or/and energy densities higher than 4-5 times ρ_0 lattice QCD calculations predict that nuclear matter consists of massless (unconfined and chiral symmetry restored) quarks and gluons. Such a state is called the "quark-gluon plasma", in analogy with the atomic plasma in which electrons become unbound from atoms. Modern cosmology asserts that this quark-gluon plasma, QGP, existed during the first few microseconds after the Big Bang. After these early instants, the Universe cooled down to temperatures below T_c^{QCD} and the plasma converted into an hadron gas before the nucleosynthesis.
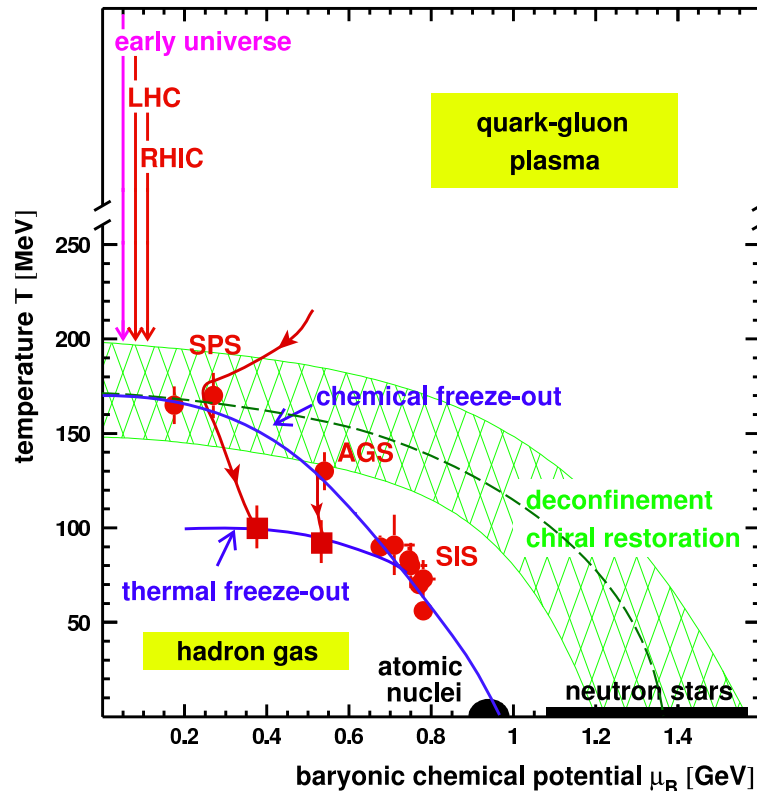
Figure 1.1: *Phase diagram of nuclear matter in the temperature versus baryochemical potential μ_B plane. The three different phases, the nuclear liquid phase, the hadron gas and the quark-gluon plasma are shown, as well as the chemical and thermal borders at freeze-out (i.e. at the points where particles do not interact through the strong interaction). From [5].*

Nucleus-nucleus collisions are the only available tool in the laboratory to explore the different domains of the nuclear phase diagram. When colliding atomic nuclei are heated and compressed reaching temperatures and pressures away from the T_0 and P_0 values of the equilibrium state, then the system evolves dynamically in a sequence of short lived states at various temperatures and preassures until it finally disassembles. Hence, nucleus-nucleus collisions provide a dynamical image of the phase diagram, i.e. no particular points of the diagram can be sampled but paths followed by the system during the reaction. The degree to which the exploration extends, i.e the sampled domain of the phase diagram, depends mainly on the variation of the bombarding energy. The higher the bombarding energy, the larger excitation energies per nucleon, $\epsilon^\star$, are reached. Nowadays accelerators as GANIL (Caen), AGOR (KVI, Groningen), SIS (GSI, Darmstadt), AGS(Brookhaven), SPS(CERN), RHIC (Brookhaven) and in the near future the LHC at

CERN, can provide in this order beam energies per nucleon, K_{lab}, of a few tens of MeV to several TeV. To set the scale, at K_{lab} below $100A$ MeV[1] the nucleus is excited up to temperatures around 10 MeV. The increase of the beam energy to $K_{lab} \approx 10A$ GeV leads to temperatures of the order of 100 MeV. Then the concept of a Fermi liquid, valid for the colliding nuclei, must be replaced by that of a hot hadron gas. Further increasing the bombarding energy above $200A$ GeV in fixed target or $20A$ GeV in the nucleus-nucleus center-of-mass, leading to temperatures above 170 MeV, the hadron gas might transform into a quark-gluon plasma.

The reaction studied in this work is inside the so-called intermediate or Fermi energy range. This domain is defined by bombarding energies of $20A$ MeV $< K_{lab} < 100A$ MeV, in which the attained excitation energies per nucleon are of the order of the binding energy of nucleons inside the nucleus ($\approx 8A$ MeV). At this bombarding region, a copious production of intermediate-mass-fragments, with charges $3 \leq Z \leq 20$, is observed for moderate excitation energies [6], $\epsilon^{\star} \approx (3\text{-}9)A$ MeV. This decay mode called "multifragmentation" is hence in between the light particle evaporation and fission, typical of lower excitation energies, and the vaporisation observed at higher excitation energies.

During the past two decades theoretical and experimental activities in this field have been stimulated by the possibility that the nuclear multifragmentation can be related with the liquid-gas phase transition [7, 8]. Figure 1.2 naively illustrates this possible connection. During an intermediate energy heavy-ion reaction, after the initial compression, the hot nuclear system expands due to thermal pressure and might enter into a metastable region reaching the *spinodal zone*. The critical/spinodal zone is the region where the derivative of the pressure with respect to the density (the compressibility), $P = \rho^2 (\partial \epsilon / \partial \rho)$, becomes negative. In this zone the system undergoes strong density instabilities and converts into the liquid-gas mixed state, consisting of droplets (the observed fragments) surrounded by nuclear gas (free nucleons and light ions)[9, 10].

Nevertheless, in the present day the origin of nuclear multifragmentation is not yet clearly understood. On the one side, statistical approaches predict that multifragmentation is a slow process and sequential fragment production caused by a thermally equilibrated source [11, 12, 13]. On the other side, dynamical models assert that the fragmenting system has not reached global equilibrium and that its disassembly is a prompt and simultaneous process [9, 14, 15]. These interpretations, which strongly differ in the prediction of the state of the emitting source and then, in the dynamics of multifragmentation,

---

[1]the A MeV unity is equivalent to MeV/nucleon
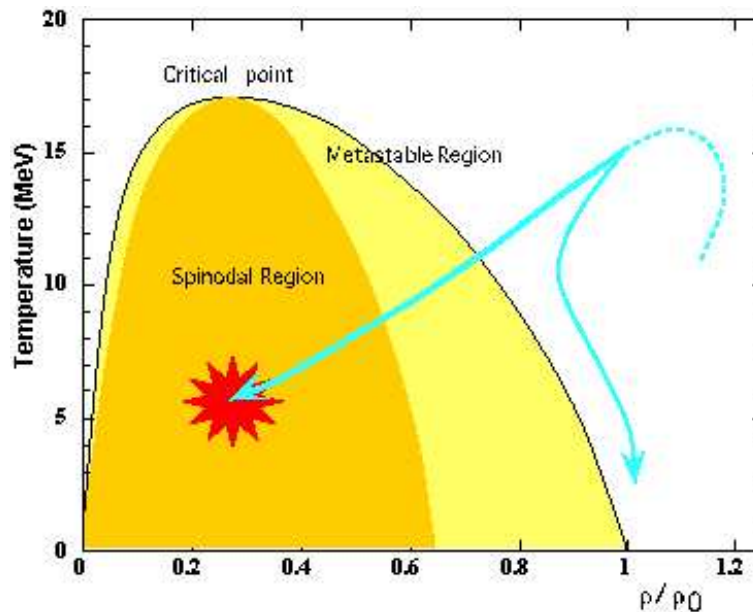
Figure 1.2: *The low temperature, low density part of the phase diagram and the critical region of the liquid-gas phase transition. The lines represent the possible trajectories followed by a nuclear system during a heavy-ion reaction at intermediate energies.*

lead to very similar results when reproducing experimental data on fragment production [16, 17]. Moreover, unfortunately, the nuclear multifragmentation is a more general process than phase transition. In the past years many investigations have been undertaken searching for different novel signals of the liquid-gas phase transition. Recently, different analyses have obtained encouraging evidences of a phase transition in nuclei which are related to experimental observations of: mass and charge distributions obeying a power law [18, 19], flattening of the caloric curve [20, 21, 22], and negative heat capacities [23] (for an enlightening summary of recent results see ref.[24]).

Despite this progress, a lot of work has to be done in order to definitely construct the phase diagram in the transition region from experimental measurements. This is an experimental challenge, mainly due to the severe experimental conditions inherent to heavy-ion reactions, reflecting the fact that colliding nuclei are finite and transient systems. The more convenient probes of the thermodynamical state of fragmenting nuclei are particles created during different stages of the reaction which are not available as initial particles in nuclei, as kaons, pions and photons. However, hadronic probes face the drawback that once they are emitted they strongly interact with the surrounding nuclear matter losing information on the phase-space distribution at its origin. On the contrary,

photons only interact weakly with the medium through the electromagnetic force, so photons are not re-scattered in latter stages after their emission, as charged particles are when suffering Coulomb or strong interactions. Therefore, photons are unique probes delivering an undisturbed image of their emitting source. Moreover, as we will see in the next chapter, photons of different energies and distributions are produced in different instants and then, at different phase-space conditions.

Outline of the thesis

The present thesis is devoted to the data analysis and to the interpretation of results of the experiment E300 performed by the TAPS Collaboration at GANIL in 1998. The main goal is to study the thermodynamical state of nuclear matter excited to the vicinity of the predicted liquid-gas phase transition. The experimental observable used in this investigation is bremsstrahlung radiation emitted from secondary nucleon-nucleon collisions at intermediate stages of the reaction.

In the next chapter the systematics of hard photon production in nucleus-nucleus collisions is summarized. We focus on the recent experimental results concerning thermal hard photon production and their connection with the present experiment. The experimental setup is described in chapter 3. The analysis of the data collected from the photon spectrometer and the charged-particle multidetectors is reported in chapters 4 and 5, respectively. The inclusive hard photon analysis is discussed and compared with the systematics in chapter 6. In chapter 7 we present the exclusive study on thermal hard photon emission. The results on thermodynamical properties of excited nuclear matter extracted from the thermal hard photon emission are presented in chapter 8. Finally, we will summarize the obtained results and proposed perspectives.

Chapter 2

Hard photon production

In this chapter the properties of bremsstrahlung photons emitted in heavy ion reactions are described. The systematics of direct hard photons is summarized in Section 2.2. The experimental evidences of the existence of thermal hard photons and the recent experimental results on thermal bremsstrahlung are presented in Section 2.3. In the last section the motivations of the experiment whose analysis and results are reported in this thesis are outlined.

2.1 Introduction: Photon spectrum measured in HI reactions

The energy of photons emitted in a heavy ion reaction depends on the underlying physical mechanism for their production and on the thermodynamical state of the system at the time of emission. Since photons do not suffer final state interactions, the momentum of a photon is not modified after its creation. Therefore, the photon energy spectrum, obtained from the addition of all photon contributions along the whole energy range, maps out the dynamical evolution of the system. The typical photon spectrum measured in intermediate energy HI reactions (Fig. 2.1) exhibits three different energy regions, each one of them is characterized by a different reaction mechanism:

- The exponential statistical contribution going from a few up to 15 MeV are statistical photons emitted in discrete nuclear transitions from the slightly excited ($\epsilon^\star \leq$ 2A MeV) reaction products present at the final stages of the HI reaction (t $\geq$ 500 fm/c).
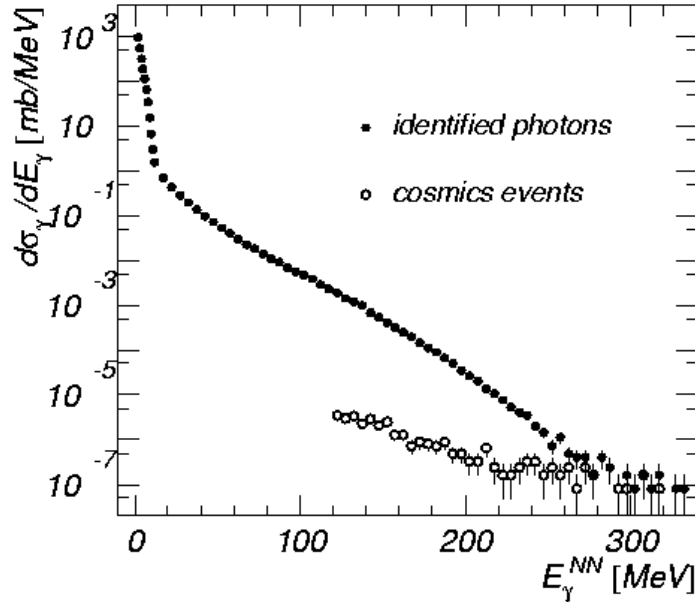
Figure 2.1: *Photon spectrum measured with the TAPS spectrometer in the NN center-of-mass for the reaction* $^{86}Kr +^{nat} Ni$ *at 60A MeV. From [25].*

- Photons of energies ranging from roughly 10 to 25 MeV are emitted during the decay of giant resonances, which are collective oscillations of all protons and neutrons within the nucleus. For the most part, this energy region is populated by photons emitted in the decay of Giant Dipole Resonances (GDRs), which are isovector electric resonances, which result from neutrons and protons oscillating in opposite phase. The spectrum measured in HI reactions in this region of energies is the result of the superposition of gamma rays resulting from the GDR decays of the hot ($\epsilon^\star \leq 4A$ MeV) quasi-projectile, quasi-target and intermediate mass fragments at the beginning of the final deexcitation stage of the nuclear reaction.

- Above ~ 25 MeV the photon spectrum is characterized by a soft exponential falloff. It mainly corresponds to photons coming from nucleon-nucleon bremsstrahlung, the so-called "hard photons".

Hard photons

The term hard photons is used in intermediate energy HI reactions to refer to photons of $E_\gamma > 30$ MeV produced in incoherent proton-neutron collisions. The maximum energy available to create a photon in the center of mass of a free nucleon-nucleon collision is $\approx K_{lab} / 2$, where K_{lab} is the incident nucleon energy. Hence, for a bombarding energy per nucleon of 60 MeV (e.g. Figure 2.1) the energy threshold of a photon created in a first nucleon-nucleon (NN) collision is ≈ 30 MeV. However photons of energies $E_\gamma > 30$ MeV are detected. The existence of these *subthreshold photons* (with $E_\gamma > K_{lab} / 2$) arises from the fact that colliding nucleons are not free but they have an additional momentum from their Fermi motion inside the projectile and target nuclei. Hard photons are therefore a unique probe of the collective properties of nuclear matter. Unlike less energetic photons, the hard photon emission is well localized at two different flashes during a HI reaction. The main hard photon contribution emerges from the early preequilibrium compressional phase at times t < 100 fm/c, whereas a softer hard photon source originates in secondary NNγ collisions produced within the nuclear fireball at t $\approx$ 100-200 fm/c [26]. The experimental hard photon spectra are well reproduced by the sum of two exponential distributions corresponding to the dominant contribution of hard photons, the so-called "direct" photons since they are produced in the leading pn collisions, and the later "thermal" hard photon contribution.

2.2 Direct hard photons

The first measurements of high energetic photons in nucleus-nucleus reactions performed in 1985 [27, 28, 29, 30] allowed to establish the bremsstrahlung origin of hard photons. Nevertheless, at that time it was not clear yet if the accelerated or decelerated particles which emitted bremsstrahlung radiation were either nuclei in nucleus-nucleus collisions or protons when colliding with other protons or neutrons. Since those first measurements up to 1992, many experiments were performed to measure hard photon observables in a wide combination of target-projectile nuclei and bombarding energies. At the same time the experimental systems were treated within theoretical frameworks [31, 32, 33] to understand the measured photon production yields. Those investigations led to the conclusion that hard photons originate mainly from the incoherent addition of bremsstrahlung radiation emitted in first-chance proton-neutron collisions. More recent investigations [34] demonstrated the direct origin of the dominant contribution of hard photons. These col-

lisions take place within the overlapping zone of the two colliding nuclei, the so-called "participant zone", during the first compressional phase. All recent experiments agree with the direct origin of the dominant contribution of hard photons. The collected direct hard photon systematics is summarized as follows:

1. **Energy spectra**

   The exponential shape of the direct hard photon energy spectrum measured in the NN center of mass is characterized by the inverse slope parameter E_0^d:

   $$\frac{d\sigma}{dE_\gamma} = K_d \, e^{-E_\gamma/E_0^d} \qquad (2.1)$$

   Experimentally it is found that the inverse slope[1] E_0^d uniquely depends on the beam energy per projectile nucleon K_{lab} corrected for the Coulomb barrier V_{Coul} between the projectile and target nuclei :

   $$K_{Cc} = K_{lab} - V_{Coul} \qquad (2.2)$$

   with the Coulomb barrier:

   $$V_{Coul} = A_{red} \cdot e^2 \cdot Z_t \cdot Z_p \, / \, R_{int} \qquad (2.3)$$

   where $A_{red} = (A_p \cdot A_t) \, / \, (A_p + A_t)$, R_{int} is the interaction radius between the projectile and target nuclei, and Z_p, Z_t, A_p and A_t are the atomic numbers and masses of the projectile and target, respectively. Figure 2.2 shows the almost linear dependence of E_0^d with the Coulomb-corrected beam energy per nucleon K_{Cc} for different experimental bombarding energies. This dependence is parameterized by the following empirical expression [34]:

   $$E_0^d = a \, (K_{Cc})^b \qquad (2.4)$$

   with $a = 0.48 \pm 0.06$ and $b = 0.91 \pm 0.03$. The fact that E_0^d does not depend on the target-projectile combination points to photon emission from individual NN collisions.

2. **Angular distributions**

   The direct hard photon angular distribution, the double differential cross-section $\frac{d\sigma}{dE_\gamma d\Omega}$, measured in heavy ion reactions can be parameterized in the source frame

---

[1]In this work I will use indifferently the terms slope and inverse slope parameter to refer to the E_0 parameter.
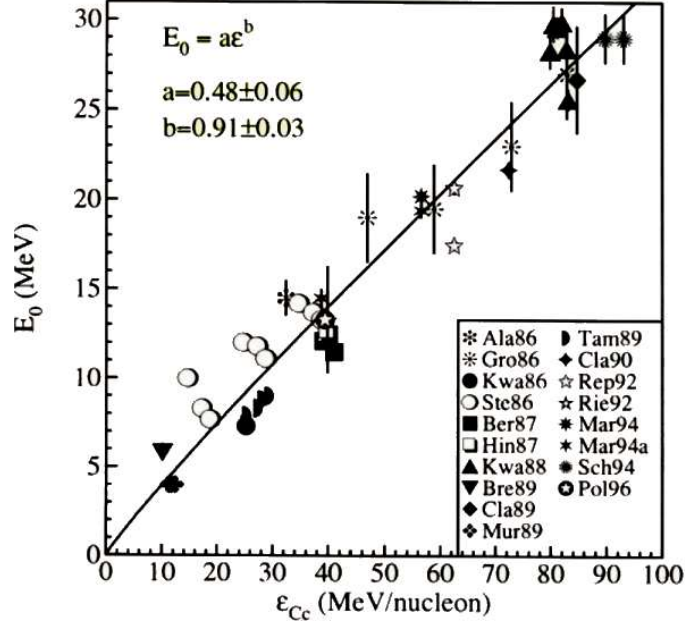
Figure 2.2: *Experimental systematics of the inverse slope parameter E_0 as a function of the Coulomb corrected beam energy per nucleon K_{Cc}. Figure adapted from the PhD thesis of J. van Pol [34].*

(NN center-of-mass frame) as the contribution of an isotropic term plus an anisotropic dipolar term [35]:

$$\left(\frac{d\sigma}{dE_\gamma d\Omega}\right)_{cm} = K^d \left[1 - \alpha + \alpha \sin^2 \theta_\gamma^{cm}\right] e^{-E_\gamma^{cm}/E_0^d} \qquad (2.5)$$

where K^d is a normalization factor and α measures the small dipole anisotropy. The existence of the dipolar term reflects the origin of the direct hard photon production. In a first-chance bremsstrahlung proton-neutron (pnγ) collision, the proton with velocity v_i is first slowed down emitting the dipolar component of the radiation, then it is isotropically scattered on the neutron and accelerated, emitting the isotropic part of the radiation, up to a final velocity v_f. Hence, projectile nucleons after this first, and hence the most energetic, collision are isotropically distributed, i.e. v_i and v_f are uncorrelated [36]. Collisions between two protons can also occur but bremsstrahlung radiation from two particles of equal charge suffers destructive interference [37] and the total almost suppressed amplitude is not of dipole type but of quadrupole type. Taking advantage of the Doppler effect, the source velocity can be extracted from the Lorentz transformation of the double differential cross-section

in the source frame to the laboratory frame:

$$\left(\frac{d\sigma}{dE_\gamma d\Omega}\right)_{lab} = \frac{K^d}{Z}\left[1 - \alpha + \alpha\frac{\sin^2\theta_\gamma^{lab}}{Z^2}\right] e^{-Z\,E_\gamma^{cm}/E_0^d} \qquad (2.6)$$

with the Lorentz factor $Z = 1/\sqrt{1 - (\beta_S)^2} \cdot (1 - \beta_S\cos\theta_\gamma^{lab})$ and β_S is the source velocity.
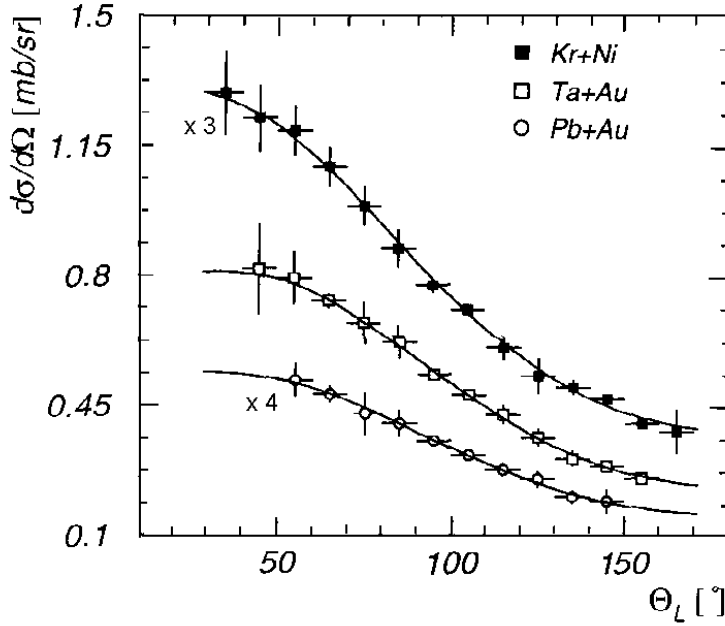
Figure 2.3: *Experimental angular distributions for photons with $E_\gamma > 50$ MeV emitted in three different reactions: $^{86}Kr +^{nat} Ni$ at 60A MeV, $^{181}Ta +^{197} Au$ at 40A MeV and $^{208}Pb +^{197} Au$ at 30A MeV. Data are fitted according to Eq. (2.6). From [25].*

The measured angular distributions in the laboratory frame are peaked in the forward direction, (see Fig. 2.3) and the anisotropy increases with the beam velocity. Fitting the angular distributions to Eq. (2.6), the extracted source velocities are very close to the NN cm velocity, $\beta_{lab}/2 = \beta_{NN}$, as expected for emissions occurring in first chance nucleon-nucleon collisions.

3. Cross sections

The experimental direct hard γ cross sections can be parameterized by the following expression [35]:

$$\sigma_\gamma^d = \sigma_R M_\gamma^d = \sigma_R \langle N_{pn}\rangle_b P_\gamma^d \qquad (2.7)$$

where σ_R is the total nuclear cross-section, M_γ^d is the number of direct hard photons emitted per nuclear reaction, $\langle N_{pn} \rangle_b$ is the number of first chance proton-neutron collisions averaged over impact parameter (the distance between the centers of the projectile and target nuclei $\equiv$ b), and P_γ^d is the probability to produce a hard photon per first chance pn collision. $\langle N_{pn} \rangle_b$ is calculated by means of the geometrical "equal-participant" model of Nifenecker and Bondorf [36], as the number of pn pairs present in the overlapping region between the target and projectile nuclei. They assume that both nuclei can be viewed as homogeneous spheres and that all nucleons in the overlapping zone collide only once. Thus, $\langle N_{pn} \rangle_b$ is parameterized by:

$$\langle N_{pn} \rangle_b = \langle A_f \rangle_b \cdot \left(\frac{Z_p N_t + Z_t N_p}{A_p \, A_t} \right) \tag{2.8}$$

with A_p, Z_p, N_p, A_t, Z_t and N_t are the mass, charge and neutron numbers of the projectile and target respectively. Here it is assumed that $A_p \leq A_t$. $\langle A_f \rangle_b$ is the geometric overlap of the colliding nuclei averaged on the impact parameter b:

$$\langle A_f \rangle_b = A_p \cdot \frac{5A_t^{2/3} - A_p^{2/3}}{5(A_t^{1/3} + A_p^{1/3})^2} \tag{2.9}$$

P_γ^d is found to depend only on the Coulomb-corrected bombarding energy per nucleon, K_{Cc} and then, due to relation 2.4, on the inverse slope parameter, according to the empirical expression [34](see Fig. 2.4):

$$P_\gamma = P_0 \, e^{-E_{thr}/E_0} \tag{2.10}$$

where $P_0 = 6.3 \cdot 10^{-4}$ and E_{thr} is the low energy threshold of the hard photon energy spectra ($E_{thr} = 30\mathrm{MeV}$).

The experimental interpretation of the direct hard photons origin is supported by theoretical calculations of dynamical transport models, mainly the BUU and QMD approaches. The BUU (Boltzmann-Uehling-Uhlenbeck) model [33] is based on a semiclassical transport equation, the Boltzmann equation, which describes the evolution of the system by a one body phase-space distribution. The Quantum Molecular Dynamics (QMD) model [14] is a time dependent A-body theory, in which each nucleon is described by a gaussian wave-function, based on a generalized variational principle. Both models describe the time evolution of the dinuclear system during the heavy ion collision, and permit to calculate the time evolution of the number of nucleon-nucleon collisions and the density of the dinuclear system.Other theoretical approaches based on hard photon production in coherent nucleus-nucleus bremsstrahlung have been proposed. However, these later do not reproduce the hard photon systematics.
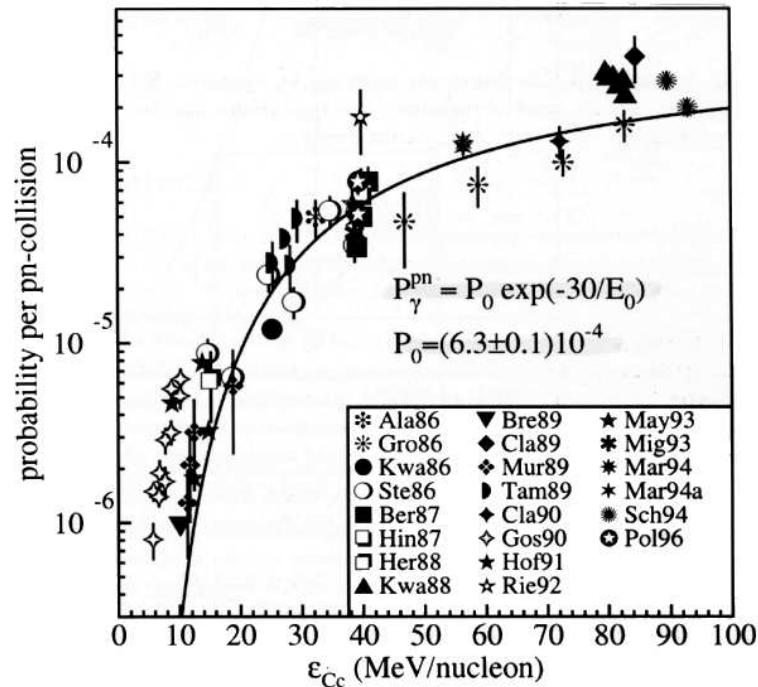
Figure 2.4: *The photon production probability versus the Coulomb corrected beam energy measured in different HI reactions. Adapted from [34].*

2.3   Thermal hard photons

The development of a second generation of photon spectrometers allowed to overcome the limited detection possibilities of those first hard photon measurements. In the experimental campaign carried out by the TAPS Collaboration in 1992 at GANIL the experimental setup consisted of the TAPS photon spectrometer, a high granularity and large solid angle calorimeter, coupled to two charged-particle detectors. The analysis of the inclusive and exclusive hard photon spectra and the two photon interference pattern [38, 39] proved the existence of an additional bremsstrahlung contribution emitted in secondary NN collisions [38, 40]. By means of a comparison of data with theoretical calculations the second hard photon source was interpreted to be in a later and thermalizing stage of the reaction [25, 41]. That investigation opened up the possibility of extracting information on the reaction dynamics and probing the thermodynamical state of the system at the intermediate dissipative stages of the reaction. Thus, those first thermal bremsstrahlung measurements motivated two experimental campaigns of the TAPS Collaboration carried out at KVI and GANIL in 1997 and 1998, respectively. The analysis and interpretation of

the collected data in the KVI experiment led up to novel results on thermal hard photon production, which are reported in the thesis of D. d'Enterria [26] and are next summarized. The analysis of the GANIL experiment is the object of the present work.

Recent results on thermal hard photon production

During the TAPS campaign carried out at the KVI facility in 1997 four different reactions, ^{36}Ar+^{197}Au, ^{107}Ag, ^{58}Ni and ^{12}C at $60A$ MeV, were studied. The consideration of these various target/projectile couples allowed to study the dependence of the hard photon emission on the size and symmetry of the heavy ion system. As for the three
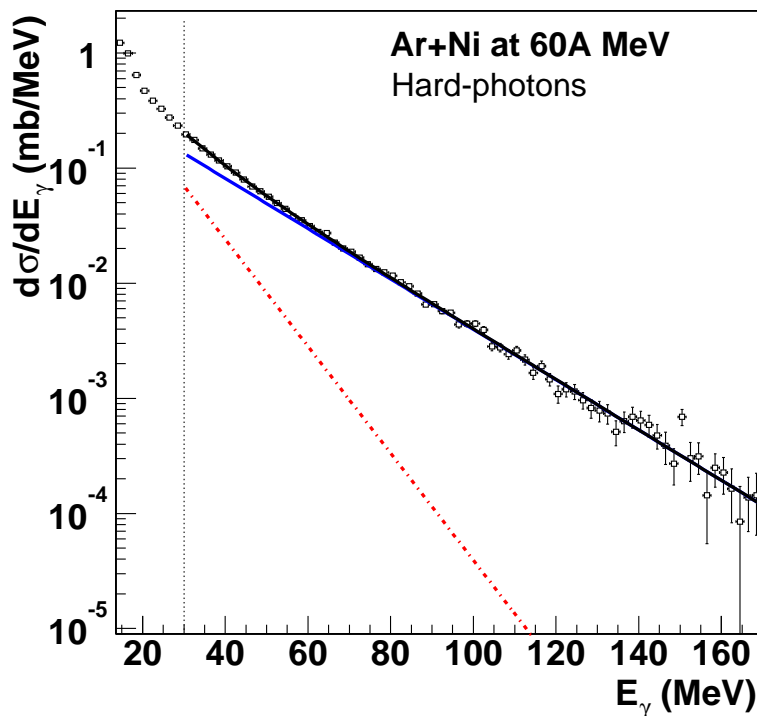
Figure 2.5: *Experimental hard photon energy spectrum measured for the $^{36}Ar+^{58}Ni$ at 60A MeV reaction. The spectrum has been fitted to the double exponential distribution of Eq. (6.2). The dotted and dashed lines represent the direct and thermal components, respectively. From [26].*

reactions studied in 1992 [40], the measured inclusive energy spectra for the three heaviest systems in the lower energy range, 30 MeV $< E_\gamma <$60 MeV, show a contribution of hard photons with a softer exponential behavior than that of the direct hard photon contribution, which follows the systematics summarized in the preceding section. The

entire hard photon energy spectra are then best described by the sum of two exponential distributions with two different inverse slope parameters, a harder slope E_0^d which follows Eq. (2.4) and a lower parameter E_0^t corresponding to the thermal hard photon contribution [40, 25]:

$$\frac{d\sigma}{dE_\gamma} = K_d \, e^{-E_\gamma/E_0^d} + K_t \, e^{-E_\gamma/E_0^t} \tag{2.11}$$

where the factors $K_{d,t}$ are defined by the intensity of the direct and thermal sources, $I_{d,t}$, respectively:

$$I_{d,t} = K_{d,t} \int_{E_{thr}=30MeV}^{\infty} e^{-E_\gamma/E_0^{d,t}} dE_\gamma = K_{d,t} \, E_0^{d,t} \, e^{-30/E_0^{d,t}} \tag{2.12}$$

2.3.1 The origin of thermal hard photons

The systematic study of the thermal hard photon production in the four KVI systems allowed to establish that "thermal" photons actually emerge from a thermalized source. This conclusion is based on the following experimental evidences:

- At variance with the pattern exhibited by the values of the direct slopes, the thermal slopes measured in the three heavier systems do not scale with the projectile energy per nucleon, but with the available energy in the nucleus-nucleus center of mass, $E_{Cc}^{AA}(A \text{ MeV}) = A_{red} K_{Cc}^{lab}(A \text{ MeV})/A_{tot}$ (A_{red} is defined in 2.2).
  This dependence points out that thermal photons emerge in a later stage of the reaction, when the initial kinetic energy has been dissipated into internal degrees of freedom as heat spread over all the dinuclear system. The measured thermal slopes are lower than the direct slopes, by a factor 2-3, reflecting that the available energy in secondary NN collisions is significantly lower than the one in leading pre-equilibrium collisions (see Table 6.2).

- Whereas the direct hard photon source moves with the expected NN cm velocity, the thermal hard photon component is emitted isotropically from a source moving with a velocity close to the nucleus-nucleus cm velocity, $\beta_S^t \sim \beta_{AA}$.

- In the ^{36}Ar+^{12}C reaction no thermal component has been observed, all hard photon production is hence well fitted with a single exponential in the energy spectrum, corresponding to the systematics of hard photons emitted in first chance collisions (see Fig. 2.6). The absence of thermal photons in this lighter system reflects the lack of volume and then, subsequent NN collisions and stopping needed to achieve thermalization.

System	E_0^d (MeV)	E_0^t (MeV)	I_t/I_{tot}	E_{Cc}^{AA}
^{36}Ar+^{197}Au	20.2 ± 1.2	6.2 ± 0.5	$19\% \pm 1\%$	7.0
^{36}Ar+^{107}Ag	20.1 ± 1.3	6.1 ± 0.6	$15\% \pm 1\%$	10.5
^{36}Ar+^{58}Ni	20.9 ± 1.3	8.8 ± 0.8	$20\% \pm 1\%$	13.4
^{36}Ar+^{12}C	18.1 ± 1.1	0.0 ± 0.5	$0\% \pm 2\%$	10.7

Table 2.1: *Direct and thermal slopes, as well as the ratios of thermal to total intensities measured for the four systems studied in the TAPS campaign at KVI. The corrected AA center-of-mass energies are also reported. Adapted from [26].*
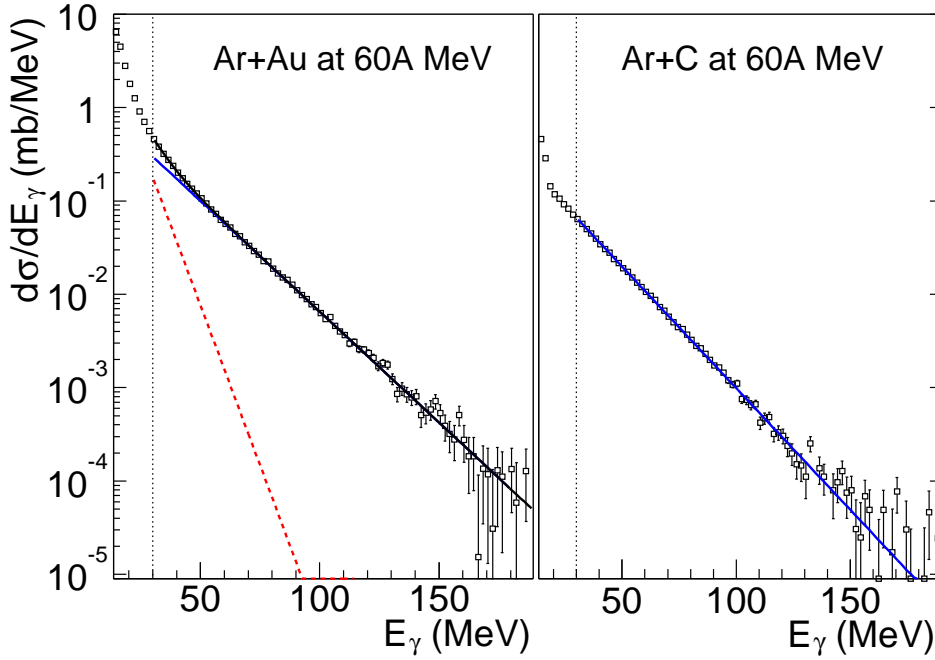
Figure 2.6: *Hard photon energy spectra measured for the $^{36}Ar+^{197}Au$ (left) and the $^{36}Ar+^{12}C$ (right) KVI systems. The spectrum of the heaviest system is fitted, according to Eq. (6.2), to the sum of a direct (solid) and a thermal (dashed) exponential distribution. The lightest system spectrum is fitted to the direct single exponential distribution of Eq. (2.1). From the PhD thesis of D. d'Enterria [26].*

- The thermal hard photon production increases with the symmetry of the colliding systems. A comparison of the measured thermal slopes and thermal to total intensity ratios (see Table 2.1) shows that the relatively most important thermal production is found not in the more massive, ^{36}Ar+^{197}Au, but in the more symmetric system, ^{36}Ar+^{58}Ni. That measurement is consistent with a thermal emission. The more symmetric the system is, the higher the energy in the nucleus-nucleus

center of mass and hence the larger the temperatures attained.

2.3.2   Multifragmentation in ^{36}Ar$+^{197}$Au reactions at $60A$ MeV

The hard photon spectrum of ^{36}Ar$+^{197}$Au reactions identified as multifragmentation events has been analyzed. The measurement of a thermal bremsstrahlung component, of slope and intensity similar to those observed in the inclusive case, proves that after the expansion phase, the system does not arrive at the low density spinodal region before fragmenting, but it undergoes a re-compression instead. In this re-compression, which is reproduced by BUU microscopical simulations, enough secondary NN collisions occur within the hot source to achieve thermalization, emitting then the observed thermal γ flash. It has therefore been concluded [42] that *at least for the* $^{36}Ar+^{197}Au$, multifragmentation is not a fast process (t $\leq$ 100 fm/c) occurring within a low density source, due to spinodal instabilities. On the contrary, the hot source breaks up after reaching thermalization (t $\geq$ 150 fm/c).

2.4   Objectives of the experiment

The TAPS campaign at GANIL in 1998 was motivated as the precedent experiment at KVI by the first thermal bremsstrahlung measurements done in 1992. The goal of the E300 experiment, performed by the TAPS collaboration in 1998 at GANIL was to investigate the thermal bremsstrahlung emission in ^{129}Xe $+^{112}$Sn reactions at $50A$ MeV, focusing on the dependence of this emission on the centrality of the entrance channel. In particular, our efforts have been focused on investigating the existence of a thermal hard-photon component emitted in central and multifragmentation reactions, for which a connection with a Fermi liquid to nucleon gas phase transition has been predicted.

The choice of the ^{129}Xe$+^{nat}$Sn system at $50A$ MeV in the proposal of the E300 experiment was motivated by several reasons:

- It is a heavy and symmetric system. The degree of excitation and the predominance of a reaction mechanism do not only depend on the bombarding energy but also on the size and symmetry of the colliding nuclei and the centrality of the collision. Therefore, nuclear systems formed in central ^{129}Xe$+^{nat}$Sn reactions are good candidates to reach the low density spinodal region.

- At $50A$ MeV the number of produced reaction fragments is observed to increase. The largest fragment multiplicities observed cannot be reproduced by the break-up of the system at saturation density with either dynamical or statistical models. The evidence of nuclear expansion is a necessary (though not sufficient) condition for the occurrence of a liquid-gas phase transition [8].

- The INDRA Collaboration has studied in detail at the GANIL facility the distribution of charged particles and related observables emitted in this reaction (see for instance [43, 44, 45, 46, 47, 48, 49] and references therein).

Chapter 3

Experimental setup

The E300 experiment was performed at the "Grand Accélérateur National d'Ions Lourds" (GANIL) located at Caen, France, during 13 days of beam time in May 1998. In this chapter the experimental setup is described. First, the GANIL accelerator complex is presented, and the beam and target characteristics are described. Next, the detector system and the features of each subdetector are discussed. And finally, we briefly describe the electronics chain and the data acquisition system.

3.1   GANIL accelerator

GANIL is an intermediate-energy heavy ion research facility operated since 1983. The accelerator system is able to provide medium-energy beams, from $100A$ down to $24A$ MeV[1] of a very large variety of ion species, from carbon to uranium [50]. As a main characteristic, the GANIL accelerator system has two identical separated sector cyclotrons in tandem (see Figures 3.1 and 3.2). Each separated sector cyclotron (SSC) consists of 4 independent magnets with C shape and 2 accelerating cavities fed by alternate voltage generators. The separated sector design allows to reach higher voltages than in conventional compact cyclotrons. And then, since the energy of the beam is proportional to the square of the radius of the trajectory, SSCs are lighter than compact cyclotrons with the same maximum energy achievements. The accelerating process at GANIL comprises the following consecutive operations:

---

[1]the maximum of the GANIL operational energy range E_{max} is only an indicative value, since it depends on the chosen beam charge state ($E_{max} \sim$ 150 Q/A (MeV/u)) and intensity.
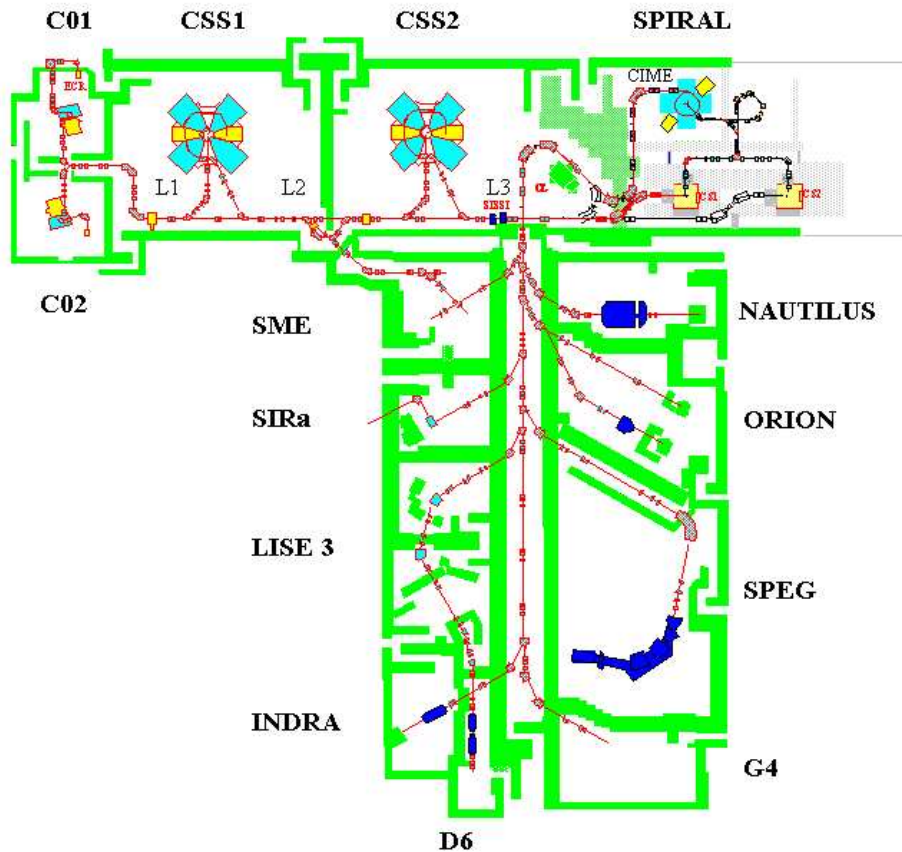
Figure 3.1: *Scheme of the GANIL accelerator system and experimental halls. Where C01 and C02 are the injectors, CSS1 and CSS2 are the separated sector cyclotrons. SPIRAL is a facility devoted to the production and separation of fast radioactive ion beams (RIBs). SME is the intermediate energy beam line, and the rest are the different detection systems. Our experimental setup was installed in the INDRA hall.*

- An Electron Cyclotron Resonance (ECR) ion source furnishes reliably the continuous heavy ion beam. Then, it is bunched in pulses of 10^5 ions each and accelerated by a compact injection cyclotron (C01 and C02 in Fig. 3.1) with a radio-frequency, RF, of 10 MHz. Hence, ions get enough kinetic energy to be injected into the first
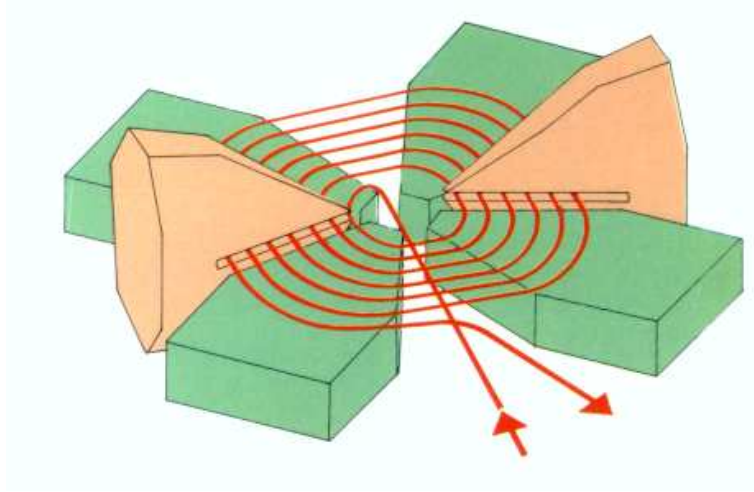
Figure 3.2: *A separated sector cyclotron (SSC). It consists of 4 magnet sectors and two RF cavities, where pulses are boosted by an electric field.*

SSC;

- In SSC1, ions with a low charge state are accelerated at an energy large enough (a factor 16 between the first orbit with radius R_i and the last with radius R_o, $R_o^2 / R_i^2 = 16$) for the next stripping process to be efficient, attaining energies of $3A$-$15A$ MeV, when the accelerated ions are ejected from SSC1;

- After exiting SSC1 the beam traverses a thin C foil which strips some of the remaining atomic electrons, thus increasing the beam charge state.

- Since the charge state of the ion beam has been raised, ions can be further accelerated by the second identical cyclotron, SSC2. After acceleration, when the beam is rejected it is analyzed by a high resolution magnetic spectrometer, and after been aligned it is directed to the different experimental halls. In our experiment the Xe beam was directed to the D5 hall ("INDRA hall", see Fig. 3.1), where the setup of the experiment was installed.

3.2 System: ^{129}Xe+^{nat}Sn at 50A MeV

The Xe beam of charge state +19 was injected into the first cyclotron with an energy of $0.55A$ MeV. After exiting SSC1 and traversing the C foil it entered into SSC2 with an energy of $7.5A$ MeV and a averaged final charge state of +46. The GANIL accelerator

Xe Beam	
A_p	129
Z_p	54
Charge state	46+
K_{lab}	$50A$ MeV
V_p	9.4 cm/ns $(\beta = 0.33)$
Cyclotron frequency	10 MHz
Intensity	5 nA
Nuclei/pulse	68
Sn target	
A_t	112
Target thickness	1 mg/cm^2
Reaction properties	
Nucl. reactions rate	$1.8 \cdot^3 Hz$
R_{int}	13.6 fm
P_{int}	$1.9 \cdot 10^{-3}$ reac./pulse
σ_R	5126 mb

Table 3.1: *Characteristics of the Xe beam and Sn target and of the $^{129}Xe+^{nat}Sn$ at 50A MeV reaction.*

system thus delivered a Xe^{46+} beam of $50A$ MeV with a nominal intensity I of 5 nA although, depending on fluctuations, beam currents reached a minimum of 1 nA and a maximum of 7.6 nA. The Xe ions were accelerated up to an energy of $50A$ MeV, this is the maximum available GANIL energy for a Xe^{46+} beam with the intensity required by the experiment. The Xe beam impinged on a ^{nat}Sn target of 1 mg/cm^2 of thickness. The choice of the target thickness t_t is an important point since on the one side, when increasing the target thickness the interaction probability, i.e. the number of nuclear interactions per pulse $P_{int}(I,t_t)$, grows and then the production of hard photons also does. But on the other side, the probability of contamination by secondary reactions and the e$^+$e$^-$ conversion probability of produced photons at the target also increase, so the target thickness has to be limited. Table 3.1 reports the main characteristics of the Xe beam and Sn target.

3.3   Detector arrangement overview

To reach the goals of the experiment an inclusive and mainly exclusive study of photon production is needed. Therefore, photons and related key observables have to be measured within a wide energy range, from statistical photons ($E_\gamma > 5$ MeV) to the hardest photons ($E_\gamma \approx 200$ MeV). Moreover, the photon detector has to offer a large solid angle coverage to allow for high quality angular distribution measurements and statistics. These requirements are completely fulfilled by the "Two Arms Photon Spectrometer" (TAPS).

To study the dependence of the hard-photon production on the impact parameter and to analyze the γ yield emitted in multifragmentation reactions, photons and charged-particle measurements have to be correlated. The detector system has hence to permit the measurement of photons in coincidence with: projectile-like-fragments (PLF), light-charged particles (p, d, t, ^{3}He, α) and intermediate-mass fragments (IMF) ($3 \leq Z \leq 20$). To fulfill these requirements, the experimental setup consisted of TAPS associated with three particle multidetectors: the GANIL Silicon Strip Detector (SSD), the Washington University "Dwarf Ball" (DB) and the KVI "Forward Wall" (FW). Fig. 3.3 shows an overview of the detector system. In the following sections each multidetector is described, since the experiment was devoted to carry out photon measurements, the characteristics of the charged particle multidetectors (which nevertheless are necessary to select different reaction classes) are only outlined.

3.4   The Two-Arm Photon Spectrometer (TAPS)

Initiated as early as 1987, the TAPS Collaboration is formed by laboratories of 5 European countries: the GSI[2] of Darmstadt, Giessen and Mainz Universities (all three in Germany), GANIL (Caen, France), the IFIC[3] (Spain), the KVI[4] (Groningen, The Netherlands) and the NPI[5] at Rez (Czech Republic). The actual objective of the Collaboration is to operate a complex and high quality device to detect and identify photons and neutral mesons, π^0 and η (by means of their decay in two photons), produced in nucleus-nucleus, proton-nucleus and γ-nucleus collisions at intermediate and/or relativistic energies (Fig. 3.4). Thus, the electromagnetic calorimeter TAPS, acronym of "Two Arms Photon Spec-

---

[2]Gesellschaft für Schwerionenforschung.
[3]Institut de Física Corpuscular.
[4]Kernfysisch Vernsneller Instituut.
[5]Nuclear Physics Institute.
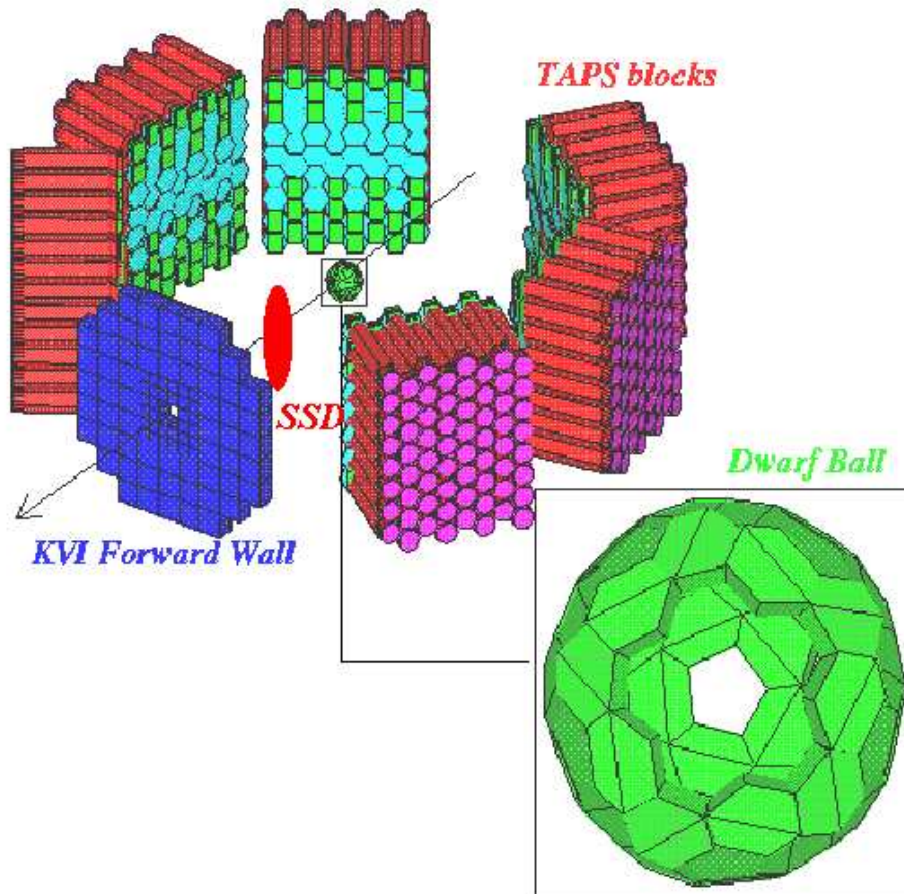
Figure 3.3: *General view of the experimental setup used to study the reaction $^{129}Xe+^{nat}Sn$ at 50A MeV. The detector system consisted of the SSD, the DB, TAPS and the FW.*

trometer"[6] is being exploited since more than 10 years. During this long period, thanks to its modularity, different detector lay-outs have been installed at many laboratories as GANIL, GSI, MAMI, CERN and KVI. The wide dynamic range of TAPS permits the detection of photons from 1 MeV to 10 GeV. These 4 orders of magnitude make this multidetector a unique tool to study very different topics in high energy and intermediate nuclear physics (see Fig. 3.4). Therefore, during the last years a rich program of experiments has been carried out: photon production in Giant Dipolar Resonances, sub-

___

[6]The "Two Arms" name comes from one of the first experimental detector lay-outs, consisting of two arms with two TAPS block each.
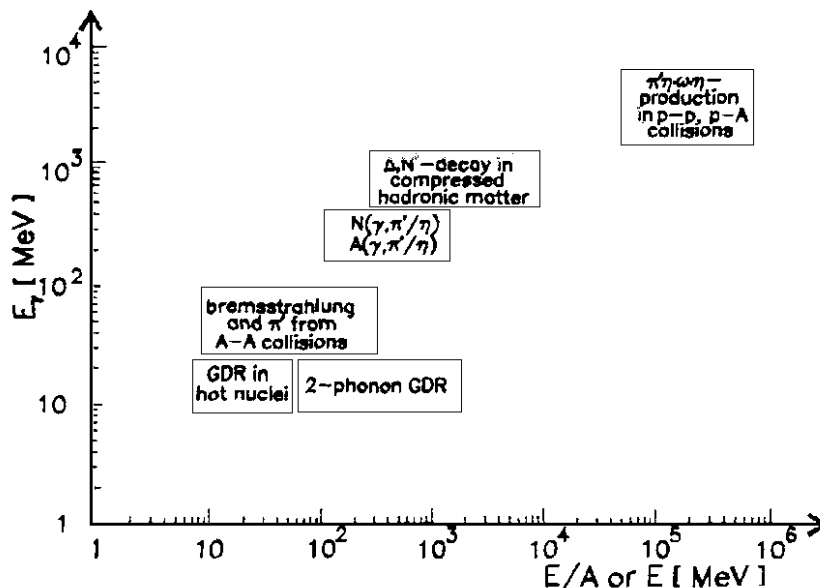
Figure 3.4: *Different physics topics addressed with TAPS[51].*

threshold π^0 production, photon interferometry, hard photon production and experiments related to baryonic excitations. A compilation of TAPS papers can be found in [52].

In the E300 experiment the TAPS electromagnetic spectrometer was composed of 384 scintillation modules. Each TAPS individual module consisted of a BaF_2 crystal and a Charged Particle Veto (CPV) detector of plastic (NE102A) scintillator. In the next section the TAPS geometrical configuration and the characteristics of the BaF_2 crystals and CPV are described.

3.4.1 TAPS configuration

TAPS modules can be arranged in several geometrical configurations, which are chosen depending on the needs and experimental conditions of each experiment. In the present experiment 384 BaF_2 modules were disposed in 6 arrays of 64 (8 × 8), (see Fig. 3.5), called blocks. The 6 blocks were placed in an almost symmetrical configuration in the horizontal plane around the target at $\phi = 0°$ and at an average distance of 56 cm. Block-target distances and relative angles θ are shown in Table 3.2. Taking into account the block geometrical configuration and each module size (see next section) the set of blocks

covered about 20% of the full solid angle[7]:

$$\epsilon_{geom} \ = \ \frac{A_{BaF_2} \ \times \ 6 \ \times \ 64}{d^2 \ \times \ 4\pi} \ = \ 0.21 \tag{3.1}$$

where A_{BaF_2} is the crystal section and d is the block-target distance.
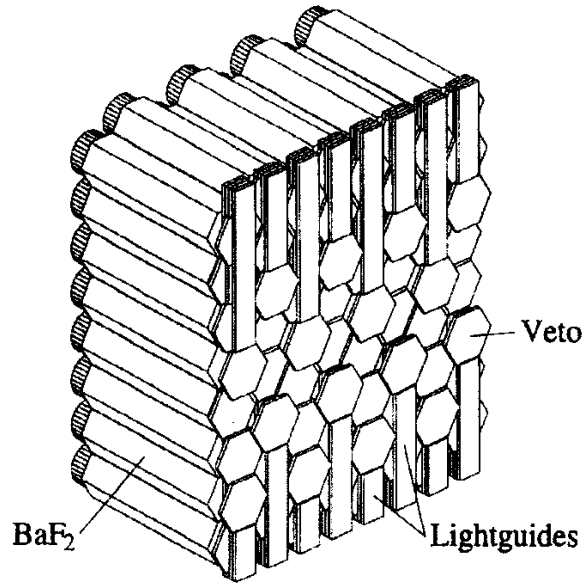
Figure 3.5: *Schematic view of a TAPS block from the front side, an array of 8 × 8 detector modules [26].*

TAPS block	Block-target distance [cm]	θ [°]
A	56.2	-50.3
B	56.0	-98.8
C	55.7	-146.0
D	56.1	152.3
E	55.9	105.4
F	56.0	57.4

Table 3.2: *TAPS block positions. Distances and angles are measured from the frontal side of each block.*

---

[7]This is only an indicative value since, as shown in the next chapter, not all BaF$_2$ worked properly.

3.4.2 BaF$_2$ crystals

The basic elements of TAPS are the 384 hexagonally shaped BaF$_2$ crystals (the main features of a BaF$_2$ inorganic scintillator are described in Table 3.3).

Crystal geometry

Each BaF$_2$ crystal (Fig. 3.6) has an inscribed radius of 2.95 cm and a length of 25 cm. As the crystal radius is smaller than the BaF$_2$ Molière radius [R$_M$(BaF$_2$) = 3.39 cm], electromagnetic showers spread out in more than one module. Hence the direction of the incident photon can be recovered with relatively good resolution by means of a shower reconstruction process (see section 4.5). The detector length was chosen to be 12 BaF$_2$ radiation lengths [X$_0$(BaF$_2$) = 2.05 cm], being then 25 cm, in order to minimize the percentage of the shower leaking out in the longitudinal direction (4% for 100 MeV photons and 15% for 1 GeV photons) [53]. Moreover, to optimize the energy resolution the modules are hexagonally shaped to maximize the number of neighbors and therefore to allow for a good shower reconstruction. The last 2.5 cm of the rear of the crystal are cylindrically shaped in order to fit to the photomultiplier.

BaF$_2$ properties	
Density	4.89 g/cm^3
Molière radius (ρ_M)	3.39 cm
Radiation length (X$_0$)	2.05 cm
(dE/dx)$_{min}$	6.6 MeV/cm
Nuclear interaction length	29.9 cm
Fast component wavelength (λ_f)	220 nm
Slow component wavelength (λ_s)	310 nm
Fast component decay time (τ_f)	0.6 ns
Slow component decay time (τ_s)	620 ns
Index of refraction	1.49 (at fast component λ_f)
Radiation damage threshold	10^7 Rads
Melting point	1280 °C
Hygroscopic	No
Hardness	3 Mohs

Table 3.3: *Properties of a BaF$_2$ crystal. Data are collected from [54].*
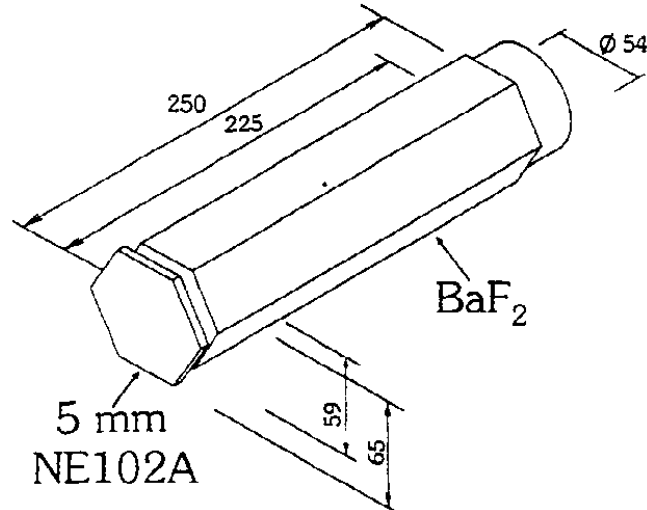
Figure 3.6: *Geometry of an individual TAPS detector module, composed of the BaF$_2$ crystal and its associated charged-particle veto (CPV). From [55].*

BaF$_2$ characteristics

BaF$_2$ had been selected as the optimal scintillation material because of its characteristic detection properties:

- The BaF$_2$ scintillation light consists of two components [56]: a fast light component with decay time of 0.6 ns emitted in the ultraviolet wavelength region of the spectrum with $\lambda_f = 220$ nm, and a slower component with 620 ns of decay time and $\lambda_s = 310$ nm. In order to observe the fast component, phototubes sensitive to the UV scintillation region, with a "quartz window" are needed. The TAPS BaF$_2$ crystals are coupled with Hamatatsu (R-2059-01) photomultipliers. One of the characteristics of this fast light component is its intensity dependence on the ionization density of the incident particle. Photons and light electromagnetic particles excite this fast component more than hadrons. Thus, the intensity ratio of the fast to the total light output is used for a first photon discrimination (the pulse-shape analysis described in section 4.3).

- Excellent time and energy resolutions. The BaF$_2$ time properties [56, 57] are due to the short decay time of the fast light component. Actually, the BaF$_2$ is the unique

high density (4.89 g/cm^3) scintillator with a light component of decay time lower than 1 ns. Therefore this is the optimal material when high detection efficiency per unit volume, and time resolution are required. Hence, for instance, when detecting photons in an environment of high neutron background the BaF$_2$ crystals allow to discriminate photons via time-of-flight analysis. Time resolutions of $\sigma \sim 300$ ps can be obtained when measuring a γ time of flight corresponding to 56 cm, (the block-target distance in our setup). As already pointed out, the crystal dimensions and shape are selected to optimize the BaF$_2$ energy resolution [58, 59].

3.4.3 The Veto detectors

A charged particle veto-detector (CPV) covers the front face of each BaF$_2$ crystal. Each CPV is made of fast plastic scintillator, NE102A, and its light output is read out by a light guide coupled to a photomultiplier. The main goal of the 384 CPV system is to discriminate between neutral and charged particles. So, the veto thickness, 5 mm, enables on the one hand, a charged particle detection efficiency of nearly 100%. And on the other hand, the conversion of high energy gamma-rays into e$^\pm$ pairs is reduced since the 5mm CPV thickness corresponds only to 0.012 radiation lengths. The vetoes are also hexagonally shaped and have a diameter of inscribed circle of 65 mm so that each veto perfectly overlaps its BaF$_2$ partner.

3.5 The charged-particle multidetectors

3.5.1 The Silicon Strip Detector (SSD)

A silicon strip detector telescope SSD (see photograph of Fig. 3.7) was placed at 19 cm away from the target inside the beam line, covering the angular range of $2.2° \leq \theta \leq 10.3°$. This device was sensitive to PLF emitted in binary reactions and IMF emitted in the forward directions from more dissipative reactions. The SSD telescope consisted of a first disc of 150 μm thickness followed by a second of 500 μm, both of them with a 68 mm diameter, and a hole of 13 mm diameter to allow the passage of the beam. The different thicknesses of the first and second stages implies also different operating voltages (40 V and 80 V, respectively) to obtain full depletion.

The association of a thin detector followed by a thick detector (the so called "telescope geometry") allows for the charge identification of particles which punch through the first

stage and are stopped in the second component of the telescope, via the ΔE- E correlation. This technique, also used in the charge identification analysis of the Dwarf Ball and Forward Wall, will be discussed in chapter 5. The first stage ΔE was composed of 64
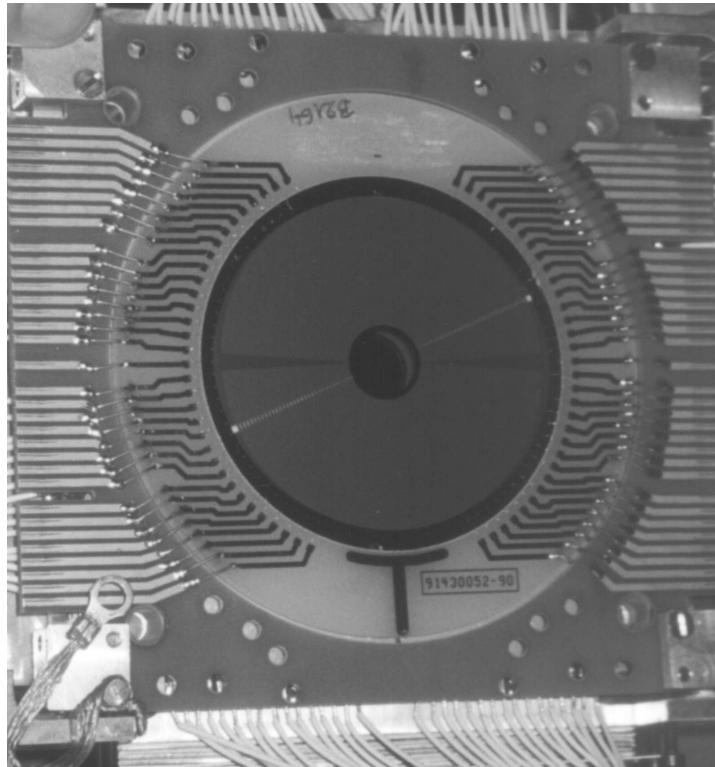
Figure 3.7: *Photograph of the silicon strip detector telescope used in our setup.*

semicircular strips with separate read out, divided into the left and right hemispheres. This circular geometry permits the location in θ (angle between the detected product and the beam line). In our experiment, the first 4 inner right and left circular strips have been rejected from the analysis since these strips are located at polar angles smaller than the grazing angle of the reaction $\theta_{graz} = 2.8°$. The second and thicker detector consisted of 128 radial strips read out also independently. The correlation of the signals of both stages with different strip geometries provides a high resolution spatial position. A general description of main characteristics of silicon strip detectors can be found in [60, 61].

SSD telescope characteristics	
Thickness of circular arrangement	150 μm
Thickness of radial arrangement	500 μm
Distance between circular strips	50 μm
Active θ coverage	$3.2° \leq \theta \leq 10.3°$
Azimuthal opening of radial strips	2.8° (full ϕ coverage)

Table 3.4: *Properties of the SSD components.*

3.5.2 The Dwarf Ball charged particle multidetector (DB)

The Washington University "Dwarf Ball" [62] was placed surrounding the target and covering an angular range of $31° \leq \theta \leq 168°$. This detector system allows to identify LCP and IMF. The Dwarf Ball (DB) consists of 64 phoswich detectors forming a sphere with an inner radius of 41.5 mm (see Fig. 3.8).

Figure 3.8: *Photograph of the Dwarf DBall.*

A "phoswich" is a detector composed of two scintillators with different decay times but readout by a common photomultiplier [63]. The light output is hence the sum of the

light emitted by both scintillators. The first and fastest (usually organic) scintillator is thin enough to allow most of the particles to punch through and to be stopped in the second and thickest scintillator, which is glued to the back side of the first scintillator. By integrating the photomultiplier output over two different time intervals or gates, the energy deposited in the first scintillator (ΔE) and the energy lost in the second scintillator, E, can be measured. As in the SSD telescope case, the ΔE - E technique is applied to distinguish and to identify the atomic number of incident particles.

DB phoswiches

In the Dwarf Ball each phoswich detector, of hexagonal or pentagonal shape (depending on the position), is made of a thin plastic scintillator and of a CsI(Tl) inorganic crystal scintillator. The plastic scintillator type (Bicron BC400 or BC446) depends on the covered angle and so does its thickness, 10 μm and 40 μm for the most backward and forward modules respectively (the positions of the DB phoswiches and thicknesses of their plastic scintillators and crystals are listed in Table B.1 of the Appendix B). The CsI(Tl) crystal glued on the back of each plastic is from 4 mm up to 8 mm thick, depending also on the angle. In each phoswich a 8 mm Lucite guide directs the plastic and crystal scintillator light to the same 6-stage photomultiplier. The plastic and the crystal scintillators, as well as the Lucite guides, are covered by a reflecting Mylar foil (150 μg/cm^2) to avoid light contamination between phoswiches. The front sides of the phoswiches are covered by absorber foils (Ta or Au) to protect against δ atomic electrons ejected from the target during the projectile passage. The thickness of these foils varies from 2.8 mg/cm^2 in the most backward detectors up to 4.9 mg/cm^2 in the most forward modules.

DB light components

The CsI(Tl) is an inorganic scintillator crystal that exhibits two light components, "slow" and "tail", characterized by different decay time constants (see Table 3.5). So the light intensity is of the form:

$$I_{CsI(Tl)} = I_{slow}e^{(-t/\tau_{slow})} + I_{tail}e^{(-t/\tau_{tail})} \tag{3.2}$$

The decay time of the "slow" component depends on the type and energy of the ionizing particle, so that the ratio I_{slow}/I_{tail} is sensitive to the nature of the incident particle. By using a pulse shape analysis, this property is exploited to identify the hydrogen (p, d, t) and helium isotopes (^{3}He, α).

By means of the definition of three proper integration time gates the intensities of the plastic scintillator signal, E_{fast}, and of the two CsI(Tl) components, E_{slow} and E_{tail},

CsI(Tl) properties	
Density	4.53 g/cm^3
Molière radius (ρ_M)	3.8 cm
Radiation length (X$_0$)	1.85 cm
(dE/dx)$_{min}$	5.6 MeV/cm
Nuclear interaction length	36.5 cm
Wavelength (λ)	565 nm
Fast component decay time (τ_f)	420 - 700 ns
Slow component decay time (τ_s)	(7000 ± 500) ns
Refractive Index	1.80
Radiation damage threshold	10^2 Rads
Melting point	621 °C
Hygroscopic	Slightly
Hardness	2 Mohs

Table 3.5: *Properties of the CsI(Tl) inorganic crystal. Data are collected from [54, 64].*

	BC-400	BC-446
Density	1.03 g/cm^3	1.03 g/cm^3
Wavelength of Max. Emission	423 nm	425 nm
Rise time	0.9 ns	0.9 ns
Decay time	2.4 ns	2.1 ns
Light output (% Anthracene)	65	64
Pulse width (FWHM)	2.7 ns	2.5 ns
Light Attenuation Length	160 cm	210 cm
No. of H Atoms per cm^3 ($\times 10^{22}$)	5.23	5.23
No. of C Atoms per cm^3 ($\times 10^{22}$)	4.74	4.74
Atomic Ratio H:C	1.103	1.104
No. of e^- per cm^3 ($\times 10^{23}$)	3.37	3.37
Refractive Index	1.58	1.58

Table 3.6: *Properties of the ΔE (Bicron BC400 or BC446) Dwarf Ball plastics. From [65]*

can be distinguished. Therefore exploiting the telescope geometry and the CsI(Tl) pulse-shape properties, one can get the IMF and the isotopic LCP identification by plotting the E_{fast} - E_{tail} and the E_{slow} - E_{tail} matrices, respectively. This analysis is presented in section 5.2.

A thorough description of the ensemble of Dwarf-Ball properties and of its associated electronics can be found in [26, 62].

3.5.3   The Forward Wall charged particle multidetector (FW)

The KVI "Forward Wall"(FW) [26, 62, 66] was designed to detect and identify light charged particles and intermediate mass fragments (up to $Z\approx15$) emitted in the forward direction. In our experimental setup this module was placed downstream at 74 cm away from the target covering the forward hemisphere behind the SSD, $2.5° \leq \theta \leq 25.°$ at a full ϕ range. The FW detector system consists of 92 plastic scintillator phoswiches. A double frame structure keeps each detector at its position and ensures the vacuum conditions by fitting the FW and the scattering chamber. The whole FW ensemble is placed in an aluminium box, see Fig. 3.9.
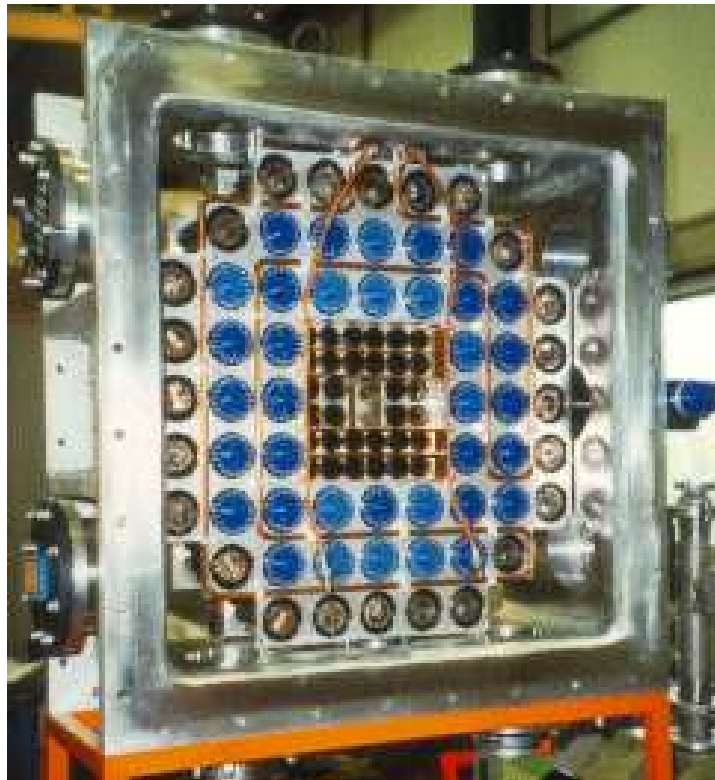

Figure 3.9: *Photograph of the Forward Wall detector.*

FW modules

Since the LCP emission is predominately forward peaked, two different phoswich sizes

are used. There is a set of 32 small phoswiches (32.5×32.5 mm^2) at the most forward angles, ($2.5° \leq \theta \leq 7.5°$), where the count rates are higher and then major granularity is needed. The remaining 60 telescopes have a larger surface, (65×65 mm^2). As in the DB case, the most forward phoswiches are covered by an absorber foil (100 μm thick Ni) in order to protect against δ atomic electrons. The small telescopes are coupled to 10-stage photomultipliers and the larger ones are readout by 8-stage or 12-stage photomultipliers. To keep good vacuum conditions the heat produced by the photomultiplier bases was dissipated by cooling the backward frame. The cooling was produced by liquid alcohol at -40°, which flowed through a small Cu pipe.

FW light components

Each phoswich is composed of two organic plastic scintillators which are heatpressed together; an 1 mm thick "fast" ($\tau = 2.4$ ns) NE102A plastic followed by a 50 mm thick "slow" ($\tau = 320$ ns) NE115 plastic. The light output characteristics of both plastics are reported in Table 3.7. By integrating the current signal delivered by each photomultiplier over two different gates one can measure the ΔE lost in the NE102A and the rest of energy E deposited in the slow and thicker NE115. As in the rest of charged particle multidetectors, the charge identification is realized by the analysis of the ΔE versus E plots.

	NE-102A (BC-400)	NE-115 (BC-444)
Density	1.03 g/cm^3	1.03 g/cm^3
Wavelength	423 nm	428 nm
Rise time	0.9 ns	19.5 ns
Decay time	2.4 ns	179.7 ns
Light output (% Anthracene)	65	41
Pulse width (FWHM)	2.7 ns	171.9 ns
Light Attenuation Length	160 cm	240 cm
No. of H Atoms per cm^3 ($\times 10^{22}$)	5.23	5.25
No. of C Atoms per cm^3 ($\times 10^{22}$)	4.74	4.73
Atomic Ratio H:C	1.103	1.109
No. of e^- per cm^3 ($\times 10^{23}$)	3.37	3.37
Refractive Index	1.58	1.59

Table 3.7: *Properties of the fast NE-102A and of the slow NE-115 Forward Wall plastics. From [65, 67].*

3.6   Electronics and data acquisition system

In each one of the 732 individual detectors of the experimental setup a particle track is identified by an amount of deposited energy inducing either a light signal in the case of a scintillator or an electric pulse in the case of a SSD strip. In order to process the resulting pulses a proper electronic chain was constructed and the physically interesting events were selected by the trigger logics. Then, pulses were processed by the TAPS data acquisition system. In this section I will briefly describe the main steps of this complex process.

3.6.1   Front end detector electronics

TAPS electronics

In Fig. 3.10 the schematic overview of the TAPS electronics chain is presented. When a light signal is produced in a BaF_2 the anode output of the firing crystal photomultiplier (PMT) is split by an AAS (Active Analog Splitter), located close to each TAPS block[8], into four pulses (Fig. 3.10):

1. One of the pulses, after being delayed by 500 ns, is fed into a Charge-to-Digital Converter (QDC). If the subevent has been accepted by the trigger logics, the signal is integrated over two different time gates, delivering hence two different energy components: *energy narrow* (E_n) from the integration of the fast scintillation component over a 40 ns narrow gate and *energy wide* (E_w) from the integration of the total light output over a time wide gate of 2 μs. This dual energy integration is the foundation of a first electromagnetic particle discrimination performed by means of the "off-line" pulse-shape analysis.

2. A second pulse is fed into a constant-fraction-discriminator (CFD) located close to the detector to avoid any possible signal distortions. If the pulse overcomes an (equivalent) TAPS energy threshold of 1.5 MeV a first logic CFD output is used as a trigger signal (CFD OR) and a second logic output, after been delayed, is split into three signals. One of them is used to start the dual gate and delay generator RDV (Retard et Durée Variables) which provides the aforementioned

---

[8]To minimize signal disturbances the first stages of the electronics chain were located only two meters away from the reaction chamber, in the D5 experimental hall
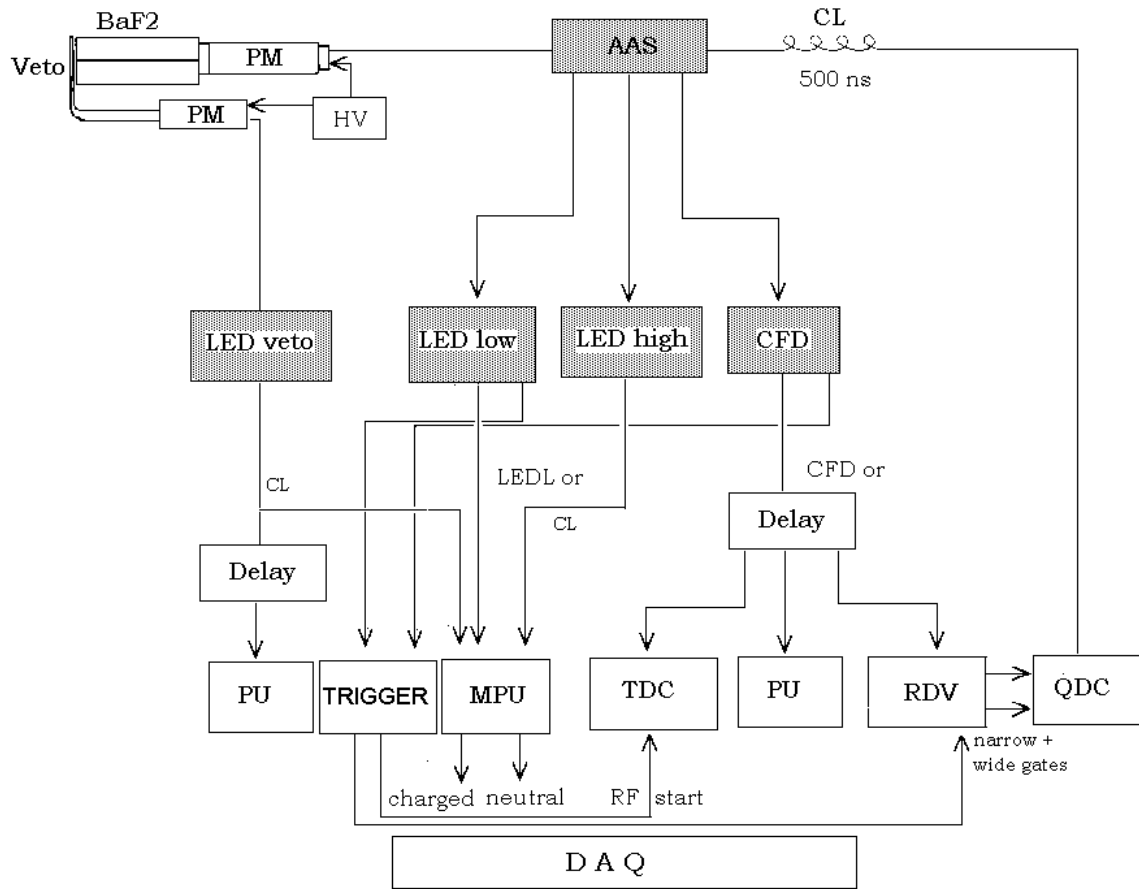
Figure 3.10: *Schematic overview of the TAPS electronics per module.*

narrow and wide gates for the QDC charge integration. The second delayed CFD
output inputs the time-to-digital converter (TDC) module, by which the time of
flight is obtained. Whereas the TDC start signal is given by a logical AND of the
accelerator radio-frequency (RF) and the master trigger, the stop is given by this
CFD output associated to the fired BaF_2. And the third logical delayed CFD output
is sent to a Bit Pattern Unit (BPU) which registers the fired BaF_2 detectors.

3. The two last AAS outputs input two Leading-Edge Discriminators (LED), LED
   low and LED high with 15 MeV and 40 MeV thresholds, respectively. The logical
   outputs of these LEDs, with also the one provided by the LED veto (see below), are
   combined in a Multiplicity and Pattern Unit (MPU). The LED-low output is also
   used as a trigger signal, i.e. there is a defined Led-low trigger (TAPS LEDL OR).

When a charged particle hits the CPV the fast signal coming from the last dynode of the veto photomultiplier is fed into a LED. The "LED veto" threshold is set approximately at an equivalent energy of 0.5 MeV (only to avoid the noise). As aforementioned, the logic outputs of the crystals and veto LEDs are grouped and, hence, charged particle hits (BaF$_2$ detector and its associated veto have been fired) and neutral particle hits (only the BaF$_2$ has been fired) are identified. This discrimination allows for a fast selection of photon events, which are correlated with information coming from the charged particle detectors by the trigger logics in order to register events of interest (see next subsection).

Electronics of the Dwarf Ball

When a charged particle impinges on one of the 64 Dwarf Ball phoswiches, the PMT output signal is amplified and split into two pulses, the *time* and the *energy* branches (see Figure 3.11). The time branch is first fed into a LED to filter the noise. This LED delivers three types of output:

1. Individual channel logic signals are retarded by up to 210 ns in an ECL delay module. They provide the stop signals for each detector in a time-to-FERA converter (TFC) module. This TFC module provides negative amplitude current pulses to the time FERA ADCs.

2. The logic common OR of each group of 16 detectors is used to create the three time gates for the energy signal integration, "fast", "slow" and "tail", and the start signal of the TFC. In addition it generates the DBOR trigger which is used in the experiment pre-trigger system. To minimize the acquisition dead-time the DBOR and TAPSOR pre-triggers are implemented without the need to go through the main trigger box. If a particular DB event is in coincidence with one of these pre-trigger conditions, and the DB system is not busy treating an earlier event, the generation of the four integration gates ("time" at t = 100 ns, "fast" at t = 170 ns, "slow" at t = 500 ns and "tail" at t = 1700 ns; each one with its own width) proceeds by default. Then, at t = 3600 ns a "fast clear" signal is produced and sent to the FERA driver. This clear signal erases all the integrated signals in the corresponding ADCs unless there exists a coincidence with the "master trigger" signal coming from the central trigger system. In this case the "clear" signal is inhibited and the FERA driver sends all the information to the acquisition through its data bus.

3. A logic signal of each individual detector for on-line monitoring purposes.

The energy branch is first delayed by 200 ns in order to wait for the gate generation and it is then split into two equal pulses with half the original amplitude:

1. One branch is used to obtain the ΔE component from the plastic scintillator in one of the 16 channel ADC FERA modules. The signal is integrated with a fast gate of 70 ns width.

2. The second branch is further split and attenuated to provide information about the slow (E signal) and the tail components of the CsI(Tl). For that, the signal is integrated twice in separate FERA ADCs: over a "slow" interval of 400 ns width and over a "tail" interval of 1.7 μs width.
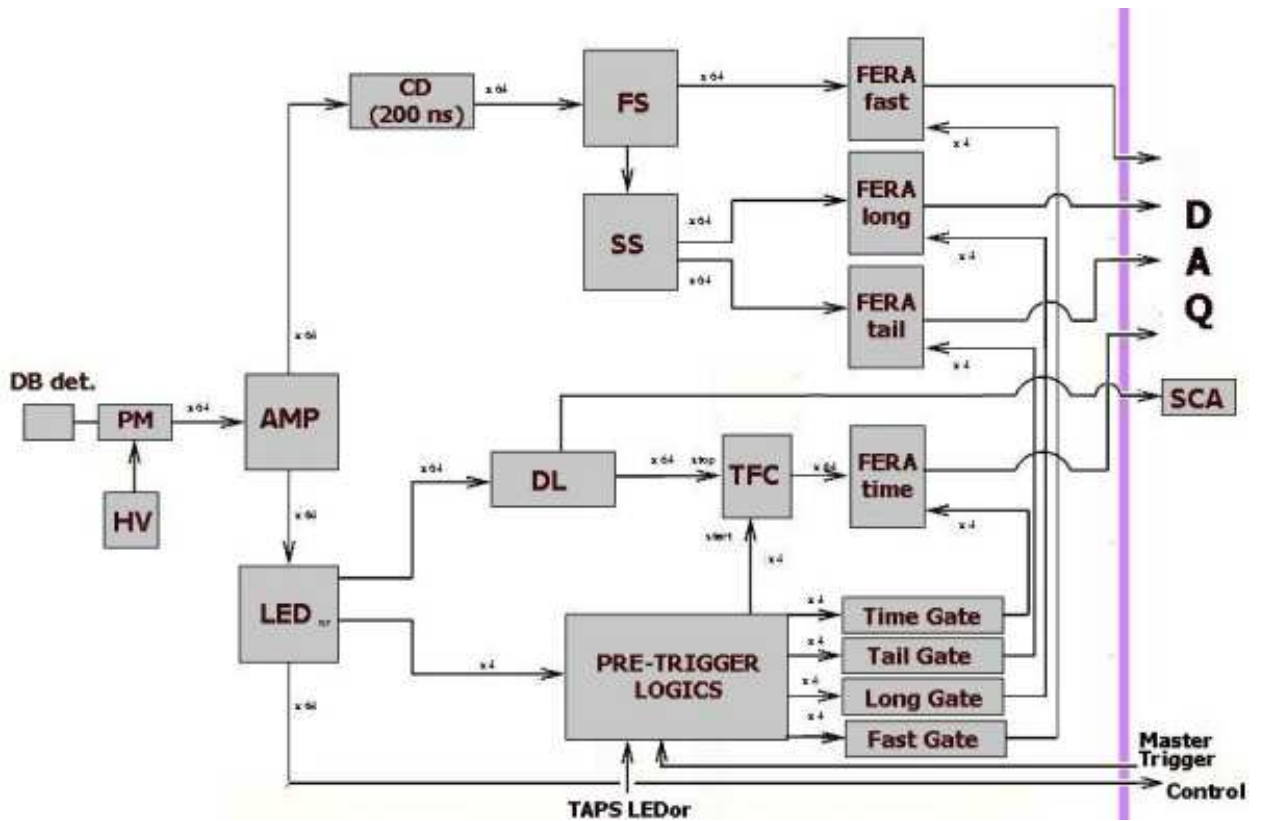

Figure 3.11: *Schematic diagram of the Dwarf Ball electronics. From [26]. A detailed scheme of the whole DB electronics and pre-trigger logics can be found in Appendix B.*

Forward Wall electronics

The analog signal from the FW module photomultiplier is first split by an AAS placed next to the hodoscope, into two branches:

1. The time-branch: The arrival of a particle signal starts the output of a CFD which is stopped by a cyclotron RF veto arriving at the same time for each group of 16 detectors. This output is subsequently delayed (by 500 ns) and sent to the counting room where it is integrated in a FERA to provide the time information of the detector.

2. The energy-branch: The analog output of the energy branch is delayed by 500 ns and sent to the counting room where it is divided into two signals which are integrated in two FERAs within two different intervals (95 ns for the "short" gate and 300 ns for the "long" one). These 2 gates are derived from the RF signal and are generated by the TAPS main trigger.
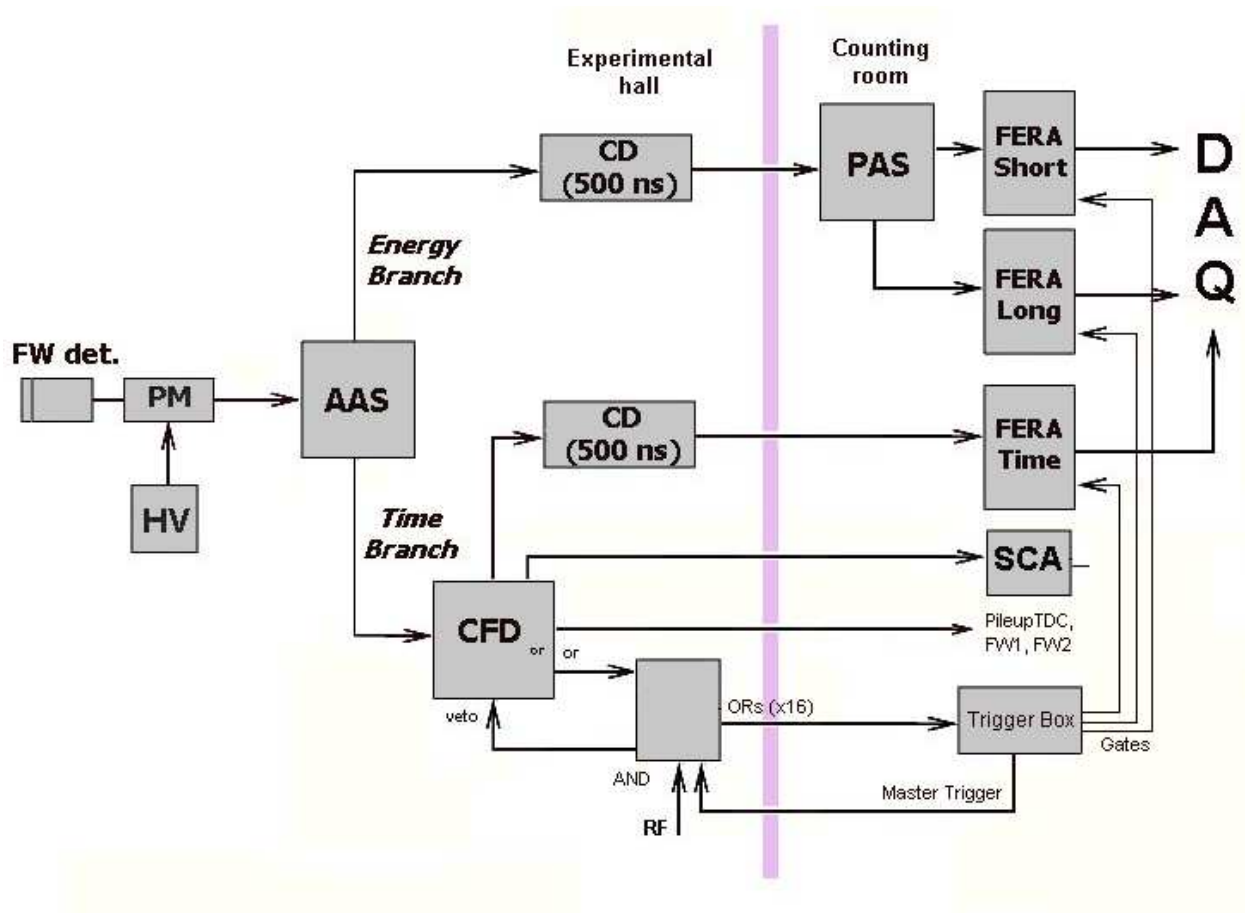

Figure 3.12: *Schematic overview of the Forward Wall electronics per module. From [26]*

Silicon Strip Detector electronics

At variance with TAPS and the two phoswich multidetectors, in the Silicon Strip Detector

(SSD) only energy signals are measured. Thus, when a charged particle hits one of the 64 circular or one of the 128 radial strips the produced slight electric signal is first fed into a multichannel preamplifier. Then, it is amplified and, if the event has been accepted by the trigger logics, it is integrated by an ADC in order to obtain the charge deposited in the hit strip. Another difference with the rest of multidetectors is that the SSD electronics was set in FASTBUS crates instead of CAMAC crates. The main features of the instrumentation needed by double stage SSDs appear in [68].

3.6.2 Trigger definition

Because of the low multiplicity in the production of hard photons, $M_\gamma \approx 10^{-3}$, the great majority, 99.9%, of occurred nuclear reactions presents no particular interest for the goal of our experiment. Moreover, the data acquisition system is only able to sustain a limited event rate, 1500 - 2000 events per second, whereas the number of produced events per second is around 18000. This difficult situation is overcome by imposing an appropiate event selection through the trigger logics. To limit the dead-time of the data acquisition, the defined triggers are down-scaled by a factor, 2^n. Table 3.8 reports the triggers used in the experiment. As a matter of fact, there were more defined triggers but, in order to avoid a still more complex electronics, the used trigger configurations were the ones strictly necessary. Some of them, CFD or, LEDL or and SSD1, were used to control the operation of various detectors but they are not exploited for the off-line analysis. As developed in chapters 6 and 7, for the inclusive charged particle measurements and the hard photon measurements the "DBOR ds" and the "neutral * DB1" triggers are used, respectively.

3.6.3 Data acquisition

The data acquisition system (DAQ) is responsible for reading all converters, building up the events (i.e. synchronizing the different *"subevents"* of the different detectors corresponding to a same reaction) and storing them in data buffers of a proper size. The data acquisition system of TAPS was used as the event builder for the whole TAPS+SSD+DB+FW setup.

The starting point for the acquisition environment of the experiment was, thus, the standard TAPS-stand-alone DAQ, and the additional DB and FW information was fed into the TAPS data stream. The TAPS converters (TDCs, QDCs and BPUs) are inserted

Trigger	Reduction factor
CFD or	$512\ (2^4)$
LEDL or	$64\ (2^6)$
Neutral	$64\ (2^6)$
Neutral * DB1	$1\ (2^0)$
Neutral * FW1	$8\ (2^3)$
SSD1	$256\ (2^8)$
FW1	$256\ (2^8)$
DBOR ds	$16\ (2^4)$

Table 3.8: *List of trigger configurations used in the $^{129}Xe + {}^{112}Sn$ experiment, with its corresponding DAQ reduction factor.*

in 13 CAMACs, each of them containing the associated electronics of half a block and also a *crate controller*, CVC. Then, TAPS subevents, built up by the CVCs, are transferred by a VME subsystem bus to two VME processors (E6A and E7A). At the same time, but faster, the converters of the charged-particle multidetectors CAMACs are read out through a fast FERA bus instead of the slower CAMAC dataway.

The total event building is performed by the TAPS DAQ. The E6A processor is responsible for collecting the TAPS, SSD, DB and FW subevents (information delivered by the charged-particle detectors is read from a Dual Port Memory by the TAPS processor) into events, which are then grouped into 8 KB buffers. Finally, another VME module carries out the recording of data-buffers on digital linear tapes (DLT). Moreover, a small fraction of the data ($\sim 1\%$) is available for online analysis which enables checking the detectors operation and the quality of the collected data.

The data acquisition system is also responsible, by means of two VME processors, of the control of the setup parameters in the high voltage units and discriminators placed in the experimental hall, as well as of the operation of the electronics at the counting room. The different VME processors are controlled, via ETHERNET, by various DEC workstations under VMS and UNIX. The software of the online analysis is run on the same workstations.

Chapter 4

TAPS data analysis

The "off-line" analysis began a few months after the end of the E300 experiment. It is a rather complex step by step process. The tapes registered by the acquisition of the experiment were sent to the CCIN2P3[1] where the data analysis of the experiment has been performed. First of all, the binary data coming from the acquisition have to be converted into physical meaningful data. Then, for each multidetector these "pre-analyzed" data have to be selected and treated in an event-by-event fashion to finally obtain the required particle distributions. An overview of this process is presented in the next section. In the following sections we will describe the analysis of TAPS data, whereas the data analysis of the charged-particle multidetectors will be described in the next chapter.

4.1 Analysis overview

The diagram presented in Fig. 4.1 summarizes the various steps of the analysis process carried out in the E300 experiment. The first step of the analysis is the decoding of raw data for all multidetectors. Each one of the $4.5 \cdot 10^8$ events recorded on tapes during the experiment is defined by a set of binary parameters delivered by the electronics of all multidetectors. The decoding process consists in recovering for each one of these buffers a list of detector channels with their associated energy and time values expressed in ADC and TDC units. This is done using a specific software package: FOSTER [70] (designed within PAW [71] framework). In addition to the decoding, the FOSTER package is devoted to the TAPS calibration and monitoring. Thus, FOSTER output run files,

---

[1]The IN2P3 (Institut National de Physique Nucléaire et de Physique des Particules) Computing Center [69], which is located at Lyon, in France.

ntuples, contain for each event the calibrated TAPS variables and the raw decoded SSD, DBALL and FWALL information. Then, the FOSTER ntuple of each run is read by
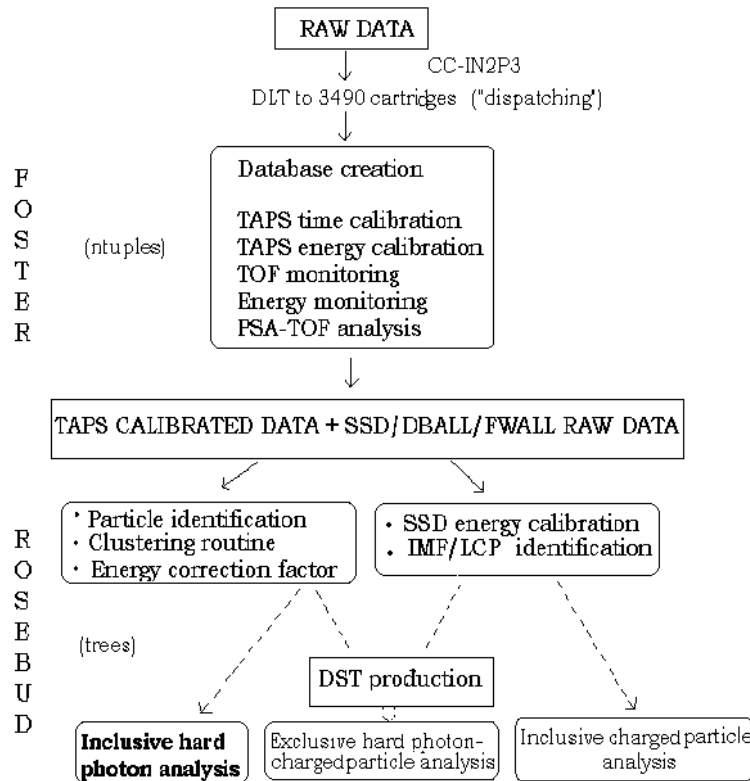

Figure 4.1: *This diagram summarizes the different steps of the analysis of the E300 experiment. In this chapter the TAPS data analysis, from the time calibration to the shower reconstruction, is described.*

the ROSEBUD [72, 73] package. This analysis software is devoted to the reconstruction of photon showers in TAPS, as well as to the raw data analysis and to the particle identification in the DBall, FWall and the SSD multidetectors. ROSEBUD is elaborated in the ROOT [74] framework and reconstructed data are stored in ROOT *trees*. Finally the produced trees, which are copied onto "Data Summary Tapes", are treated by the histogram programs to get the physical results.

In the next sections the TAPS data analysis is described: from the time and energy calibration, and its monitoring, to the photon shower reconstruction.

4.2   TAPS calibration and monitoring

The TAPS pre-analysis performed with FOSTER consists, after decoding, in transforming each one of the TAPS raw parameters, measured in channels, into physically meaningful quantities. The measured time is converted into *ns* and both energy components, E_w (w stands for wide gate) and E_n (n stands for narrow gate), are converted into MeV. Then, this calibration is monitored and the γ times of flight are aligned. In summary, the different steps of this TAPS pre-analysis are:

- The time-of-flight (TOF) calibration and monitoring;

- The energy calibration and monitoring;

- The time of flight correction;

- The analysis of the pulse shape versus time of flight, PSA - TOF.

An appropriate detector calibration must take into account that variations in the experimental conditions can occur during the experiment. These variations may modify the detector response and, as a consequence, a unique calibration can not be performed. Therefore, a calibration procedure was applied to each one of the 45 run sets in which the E300 data were segmented. This segmentation was done taking into account the different beam-off periods, intensity fluctuations or possible detector gain shifts. Beside this in-beam run division, during the experiment 7 different out-of-beam run sets, a total of 27 runs, were written on tape. As we will see in subsection 4.2.3, the analysis of these sets of out-of-beam runs has been very useful.

4.2.1   Time-of-flight calibration

For every beam burst, whenever a projectile-target collision producing a photon takes place, the corresponding TOF structure presents two bumps (see Fig. 4.2): a prompt peak corresponding to photons and a minority of electrons traveling at relativistic speed ($\sim$ channel 600 for our illustrative example) , and at larger time-of-flight values, a broad bump due to hadronic massive particles. A comparison of Fig. 4.2 and Fig. 4.3 shows that the particle statistics of a detector in block A is slightly larger than the one of detectors of block D. This is due to the relative angular position of these blocks; light charged particles are produced mainly in the forward direction, where blocks A and F are
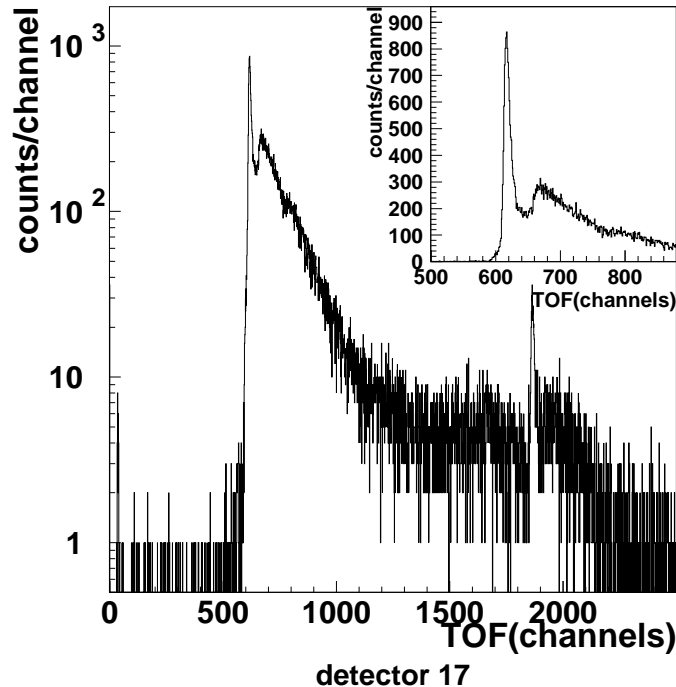
Figure 4.2: *Illustrative time-of-flight spectrum (detector 17 in block A) corresponding to a set of 50 runs. The inset shows a zoom of the same spectrum with a linear y scale to emphasize the γ peak.*

positioned, while the number of particles produced at larger angles with respect to the beam direction is strongly reduced. Thus, the statistics of a detector in block C or D, covering the backward region, are lower.

The periodicity of the GANIL beam is exploited in order to calibrate in time the TAPS modules. The time difference between two consecutive beam bursts is 100 ns, the inverse of the cyclotron radio frequency $RF = 10$ MHz of the Xe^{46+} beam. The TAPS TDC range is chosen to be large enough in order to record reactions occurred in two consecutive beam pulses. So, in our experiment there are two prompt peaks and two particle bumps in each TOF individual spectrum (Fig. 4.3).

The time calibration is done using the position in time of the two recorded consecutive prompt peaks corresponding to each beam burst. The first prompt peak is expected to be at 1.87 ns, since this is the time needed for a photon to traverse the target-TAPS module distance, 56 cm. While the second prompt peak will be at 1.87 ns + 100 ns. In the time
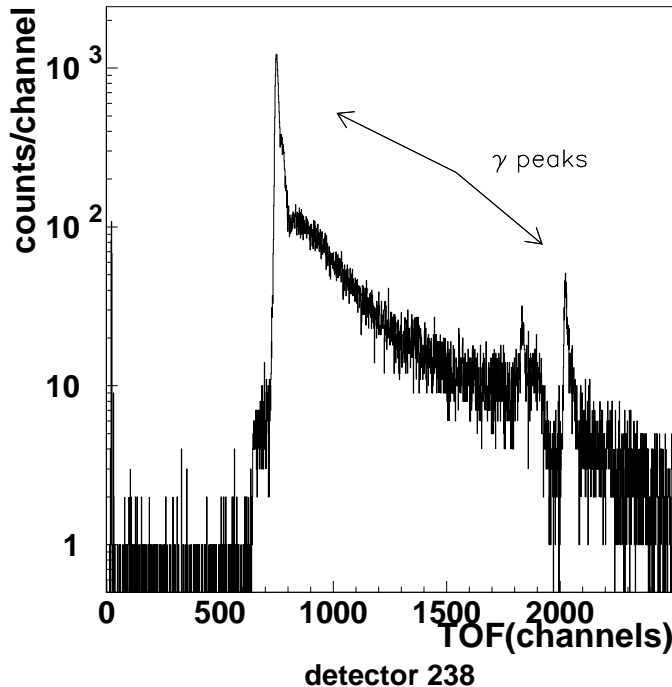
Figure 4.3: *Time-of-flight spectrum of detector 238 (in block D) corresponding to a set of 50 runs.*

calibration procedure, a FOSTER macro generated a HBOOK file for each set of runs with the time-of-flight spectrum of each detector. Then, for each individual detector, and for each calibration set, the two prompt peaks were located, and the detector gain, F_G, was calculated, using the time separation between the prompt peaks. For each run set we generated a file containing the first prompt peak position, F_o, and the gain of each detector. Finally, the database was updated so that FOSTER could transform through these files the raw time into calibrated time (see Fig. 4.4), using for each BaF_2 detector the following expression:

$$TOF_i^{cal} = (TOF_i(raw) - F_{o_i}) \times F_{G_i} + 1.87ns \qquad (4.1)$$

where i = 1,..., 384. We found that the averaged gain of the 384 detectors was about 80 ps/channel and the gain dispersion for the different set of runs was smaller than 20 ps. Nevertheless, this division in set of runs helped us to detect 13 detectors which performed improperly along different run sets.
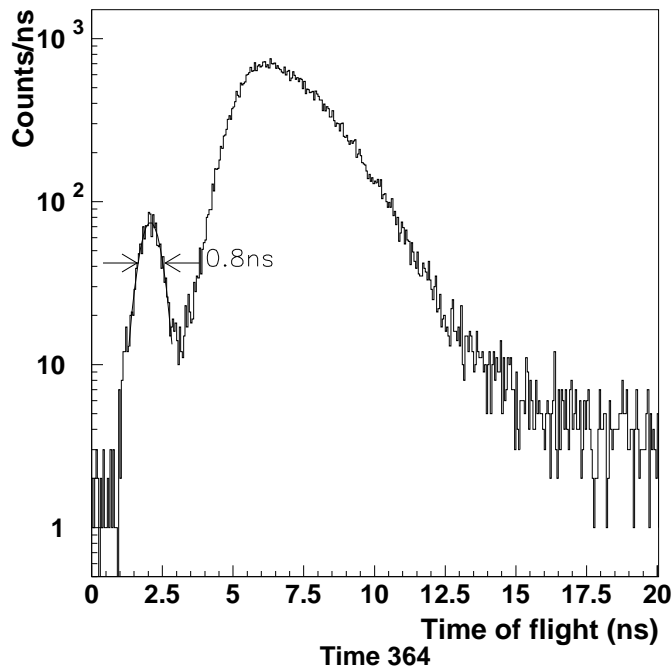
Figure 4.4: *Calibrated time-of-flight spectrum of detector 364. It shows the prompt peak and the broad bump of slower hadronic particles. The FWHM of the photon peak, after time corrections (see next section) is 0.8 ns and hence the time resolution $\sigma = 340$ ps.*

4.2.2 Photon TOF correction

The only means to distinguish the photon signal, which we are interested in, from neutrons is comparing their different time-of-flight. Therefore, it is necessary to get as much precision as possible when locating the γ prompt peak in order to separate unambiguously these neutral particles. In oder to do so, we have to take into account and correct the deviations of the photon peak away from the 1.87 ns value. These deviations result mainly from RF drifts and walk effects [38].

RF drift

During the long period of the experiment the GANIL accelerator system encountered modifications in its operation parameters. Thus, the cyclotron RF had instabilities, not only small fluctuations but also falls and jumps each time the beam was stopped for some moments. As the START signal was given by the correlation between the RF accelerator

signal and the master trigger, these RF drifts, and also, but with a less important effect, electronics delays, led to fluctuations in the photon peak time position. These deviations were corrected, after the time calibration, with the FOSTER time monitoring routine.

Every 10^5 events, corresponding to a few minutes of data acquisition during the experiment at nominal beam intensity, ~ 1000 event/s, a time-of-flight spectrum is generated and the position of the photon prompt peak (see Fig. 4.5) and its width are monitored. And also, the difference between the real and the expected photon peak position, $t_0 = 1.87$ ns, was automatically calculated. Then, for every run, a TOF shift calibration file containing these differences was generated in order to align the photon peaks at the reference value, t_0. Once the database was updated, including these time shifts, the corrected γ prompt peaks, the flatter line of Fig. 4.5, were centered at 1.87 ns and exhibited a width evolution lower than 0.2 ns. We have to note that the big spikes present in the uncorrected TOF γ peak spectra come from events without beam, recorded during the accelerator failures. Then, the corresponding runs were discarded from the analysis, so they do not appear in the corrected time monitoring spectrum.
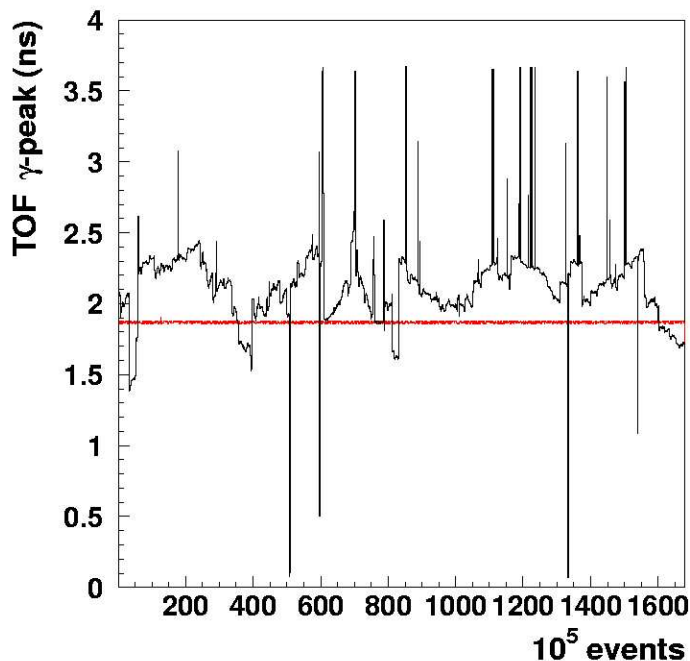

Figure 4.5: *Evolution of the position of the γ peak, before and after the HF drift correction. Runs without beam are eliminated from the corrected photon peak position spectrum.*

Walk effects

The response of the CFD, which delivers the stop of the TDC, does not depend in principle on the height of the input signal. However to correct for possible walk effects, i.e. two signals of different amplitude but rising at the same time may trigger the discriminator in two different times, 6 energy domains are taken into account in the photon identification procedure: $E_w < 5$ MeV, 5 MeV$< E_w <10$ MeV, 10 MeV$< E_w <20$ MeV, 20 MeV$< E_w <60$ MeV, 60 MeV$< E_w <100$ MeV and $E_w >100$ MeV.

4.2.3   Energy calibration

As for the time signal, the first task when dealing with the energy signals delivered by the two integration QDC gates is the calibration. The conversion of the two energies, E_n and E_w, measured in channels into energies expressed in MeV is done taking into account that the fast BaF$_2$ response is linear [53, 59]. Thus, for each module the following expression is used:

$$E_i^{cal}[MeV] = Gain_i[MeV/channel] \cdot (E_i[channel] - pedestal_i[channel]) \qquad (4.2)$$

with i $= 1,..., 384$.

Pedestal

The pedestal is the first left not empty channel of the QDC spectrum. It is the response of the QDC without any input signal from the multiplier. So, this value, the corresponding channel, depends on the intrinsic charge of each module, as well as on the cable noise.

Gain

We take advantage of the known amount of energy deposited by the cosmic μ background to determine the gain of each TAPS crystal. The interaction of primary cosmic ray protons when arriving at the atmosphere with the nuclei of the air molecules induces the formation of secondary particles (mainly pions). Next, atmospheric charged pions decay into muons ($\tau = 26$ ns), which arrive on the ground. Although its short life-time, $\tau = 2.2$ μs, muons can arrive at the earth surface without decaying into electrons because of its high energy, 2 GeV on average [75]. This high energy also makes cosmic muons
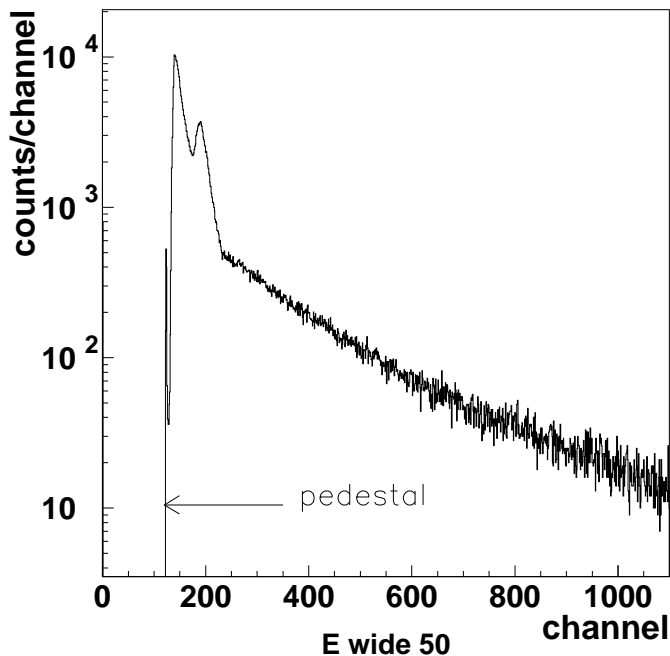
Figure 4.6: *Raw energy wide gate spectrum of module 50 measured during 30 beam-on runs. A comparison with Figure 4.7 shows that about the position where the cosmic peak is expected to be, the background is quite important.*

interact as minimum ionizing particles (MIP), i.e. the amount of lost energy per path length which only depends on the nature of traversed material and not on the energy of the incoming particle. In the case of BaF_2 crystals the deposited energy per 1 cm path length is 6.6 MeV [76]. Thus, taking into account the vertical size of a TAPS module, the total energy that a muon loses when traversing vertically a TAPS crystal is calculated to be 38.0 MeV. Since the BaF_2 crystal response depends on the mechanism by which incident particles excite its structure, i.e. on the nature of the incoming particle, this energy calibration will be only valid for $e^{\pm}$ and photons whereas for hadrons it will be only indicative. However, since cosmic muons lose their energy ionizing the crystal while photons develop electromagnetic showers, photon energies have still to be corrected for the μ and γ differences in the light production efficiencies (see section 4.6).

As already discussed, we only need two parameters to calibrate the BaF_2 detectors, the pedestal, i.e. the 0 MeV point, and the gain. The normal energy calibration procedure, used in previous experiments at KVI [34, 73, 77, 26], consists of applying the FOSTER

calibration routine for each one of the sets of in-beam runs, as it has been already done for the time calibration. As cosmic events are recorded in random coincidence with events coming from nuclear reactions, the energy spectra present a Gaussian shaped peak corresponding to the amount of energy deposited by cosmic μ. Thus, for each one of the 384 BaF_2 modules, and for each set of in-beam runs, the pedestal and cosmic peak for E_n and E_w spectra can be located. Nevertheless, in our experiment we could not use this
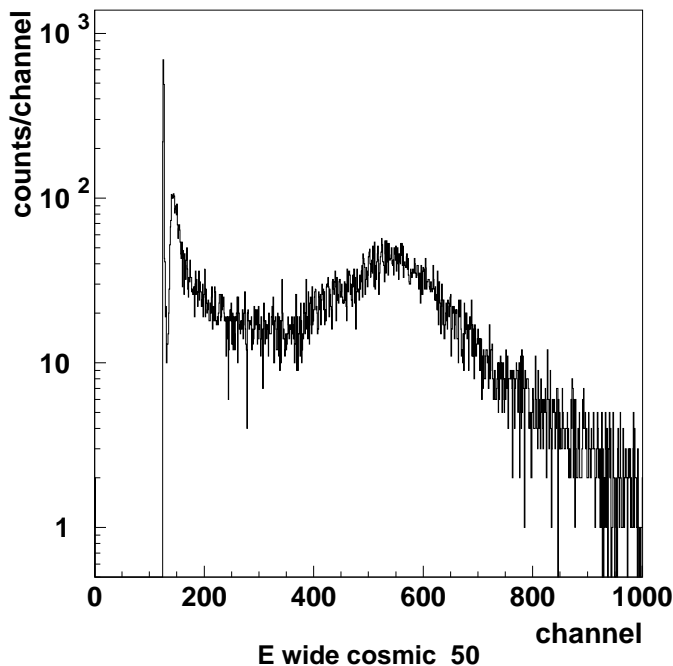

Figure 4.7: *Energy wide gate spectrum of module 50, corresponding to a set of cosmic runs.*

procedure during in-beam runs, since the cosmic peak could not be well distinguished from the background, (see Fig. 4.6). It was still impossible even when we tried to construct the energy spectra selecting TOF zones where no reaction products were expected. But at these larger TOF values, after the broad particle bump, the μ zone could not be well identified either. The cause of this impossibility was that at the GANIL facility the beam was stopped inside the experimental hall D5, whereas the relatively lighter KVI beam was stopped outside the experimental hall, and as consequence the neutron background was specially low at the former KVI experiments. This is also the reason why a cosmic trigger was not used in our experiment, this trigger has been defined in other TAPS experiments to record beam-on μ events to be used for the energy calibration. Since

neutrons of the background between pulses would also have been accepted by the cosmic trigger. Therefore, an alternative calibration method was applied using 4 sets of out-of-beam runs. As aforesaid, these runs were recorded during different beam-off periods. Fig. 4.7 shows an energy wide gate spectrum accumulated during some of these beam-off runs. The peak of the bump corresponds to the energy deposited by muons which have traversed vertically the module 50, while the rest of the structure is due, in the main, to muons with different inclined trajectories. Thus, for each detector and for the two energies, a fitting routine was used in order to locate the μ peak as the center of a Gaussian + first order polynomial distribution. Then, the gain of each BaF$_2$ crystal i was calculated from:

$$Gain_i(MeV/channel) = \frac{38.0(MeV)}{cosmic\,peak_i(channel) - pedestal_i(channel)} \qquad (4.3)$$

The average gains for different modules are between 75 keV/channel and 85 keV/channel, but the lower and upper limit of measured gains are 23 keV/channel to 360 keV/channel, respectively. However, the gain of each module only varied slightly, less than 4%, from one cosmic run set to another. So that the energy calibration could be done for the different sets of in-beam runs taking the gains of the nearest set of beam-off runs.

4.2.4   Energy monitoring

In order to check the validity of the energy calibration and to locate possible important gain drifts we performed an energy monitoring. This procedure consisted in monitoring the slope of the proton contribution in the calibrated energy spectra for 17 different energy sets od runs, see Fig. 4.8. The slope was calculated for each detector from an exponential fit between 40-80 MeV. We were not interested in the proton energy but in possible changes of the proton energy slope as indicators of possible detector gain drifts.

As a matter of fact, since the wide energy component is the total energy left by a particle, we were interested in possible fluctuations in this component since they would affect the photon energy measurements. As it is the case for the detector of Fig. 4.9, the value of this slope remained constant for most detectors, indicating that gains of BaF$_2$ crystals were stable. Although for modules of the backwards blocks this monitoring was less significant, due to the aforesaid low particle statistics obtained for these blocks. As in the time calibration procedure, the output of the energy spectra of each module allowed us to localize a few modules, 8, with problems, whose data were discarded. Therefore, taking into account also the modules with a deficient time response, a maximum (the
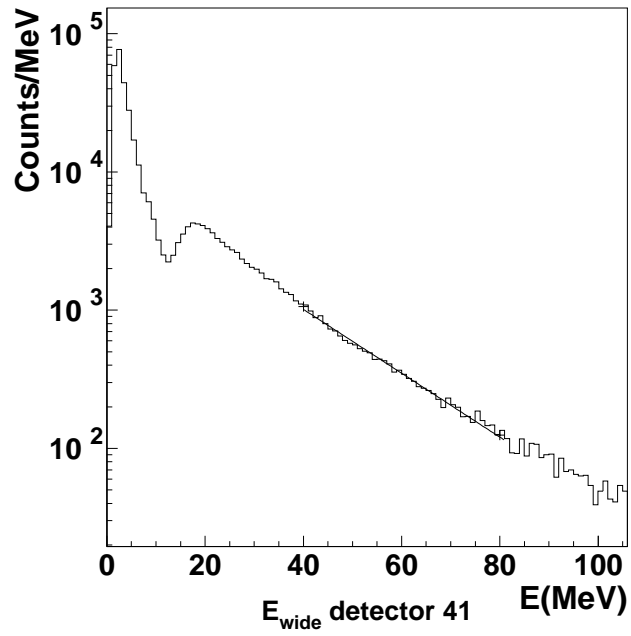
Figure 4.8: *Energy wide spectrum of module 41. The spectrum has been fitted between 40-80 MeV, (solid line), to extract the particle slope.*

number varies slightly depending on the set of runs) of 23 detectors were rejected from the analysis.
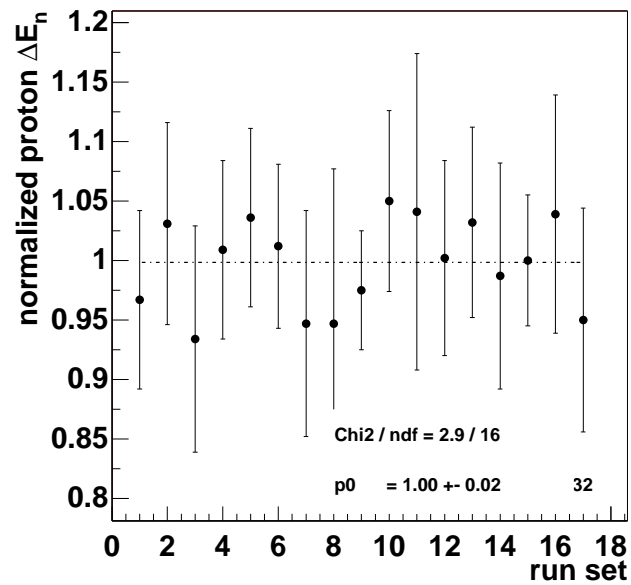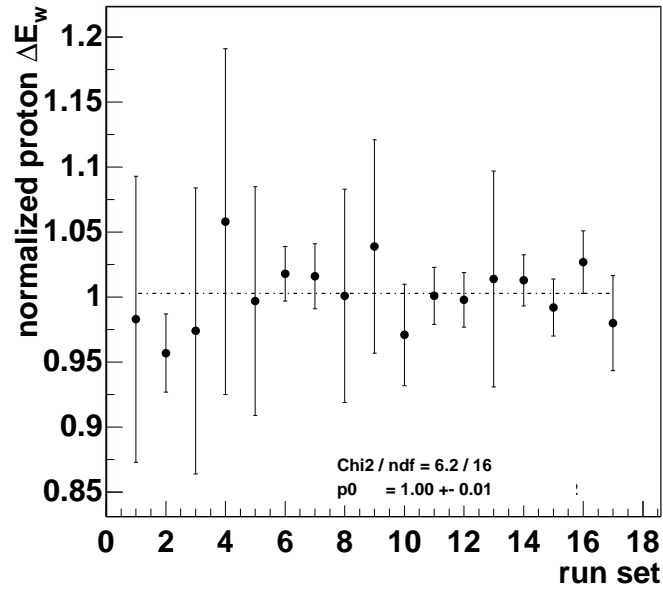
Figure 4.9: *Normalized proton ΔE of the same detector of Fig. 4.8 for the different run sets.*

4.3   PSA-TOF analysis

The PSA-TOF analysis allows on the one hand to check the all previous time and energy calibration and monitoring tasks. On the other hand, it is a method to discriminate unambiguously photons from incident hadrons. This discrimination is a first condition in order to identify the electromagnetic showers induced by photons. We define PSA as the ratio of calibrated E_n to the total calibrated light output, E_w, in order to compare the relative energy intensities induced by the different particle species (electromagnetic and hadronic).
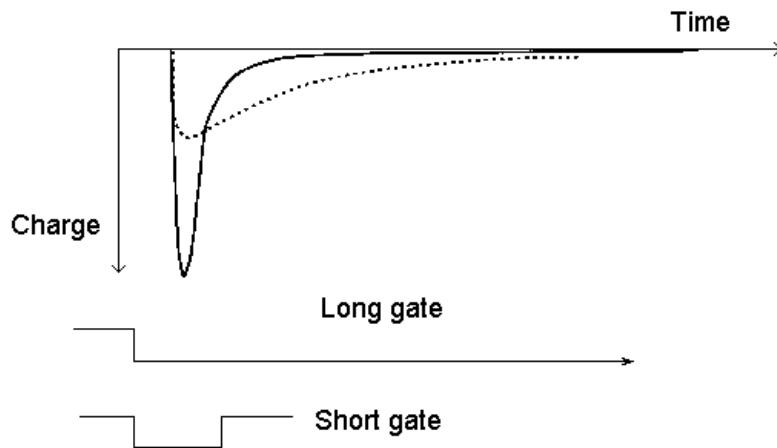

Figure 4.10: *Typical BaF$_2$ pulse shape induced by a photon (solid line) and by a proton (dashed line).*

As we have discussed in 3.4.2, the two different scintillation components of a BaF$_2$ crystal, differ in their decay times and scintillation efficiencies. And, as other inorganic scintillators (e.g. CsI and NaI), the relative intensity of these two energy components depends on the incident particle nature, more precisely on its ionization density [78, 58]. Photons and leptons ($e^{\pm}$, $\mu^{\pm}$) induce a stronger intensity of the fast component than the one caused by hadronic particles, see Fig. 4.10. Thus, the PSA generated by photons, electrons and muons is centered at 1. Protons, neutrons, alphas and the rest of heavier particles excite relatively less the fast energy component, so its associated PSA is lower than 1, e.g. it is centered at ~ 0.7 in the 20 MeV$<$ E$_w$ $<$60 MeV energy range.

We also take advantage of the excellent time resolution of the ultraviolet scintillation

light of the BaF$_2$ crystals to measure the TOF of the different types of incident particles. As we have seen in the time-calibration section, photons and relativistic leptons, as fast particles, are located in time within the prompt peak, centered at TOF $= 1.87$ ns. Whereas heavier particles have a greater TOF, whose value depends on the energy of the incident particle.

Therefore, a bidimensional plot of PSA versus TOF will show different regions corresponding to the different types of particles. The PSA-TOF plots have been generated for 6 different total energy (E_w) domains, covering all the energy range. Fig. 4.11 and Fig.4.12 show PSA-TOF plots consisting of all BaF$_2$ detectors for the energy ranges of 20 MeV$<$ E_w $<$60 MeV and 60 MeV$<$ E_w $<$100 MeV, respectively.
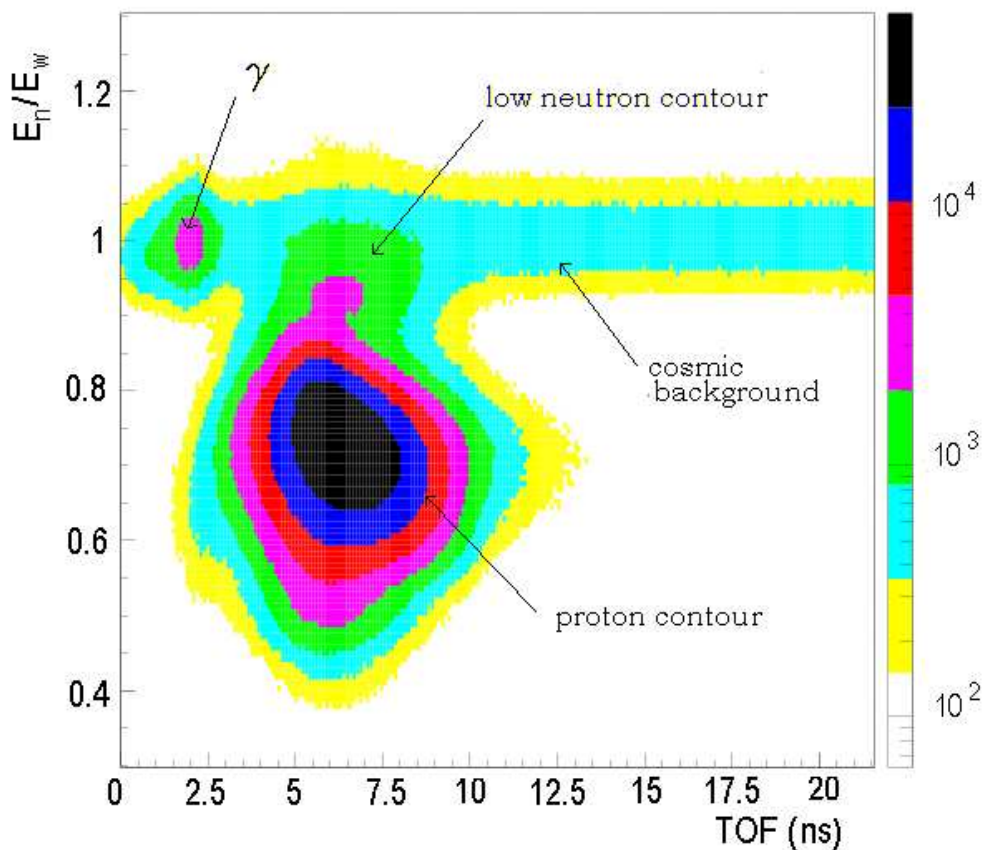

Figure 4.11: *PSA versus TOF summed for all TAPS modules, and considering all particles with deposited energies of 20 MeV$<$ E_w $<$60 MeV.*
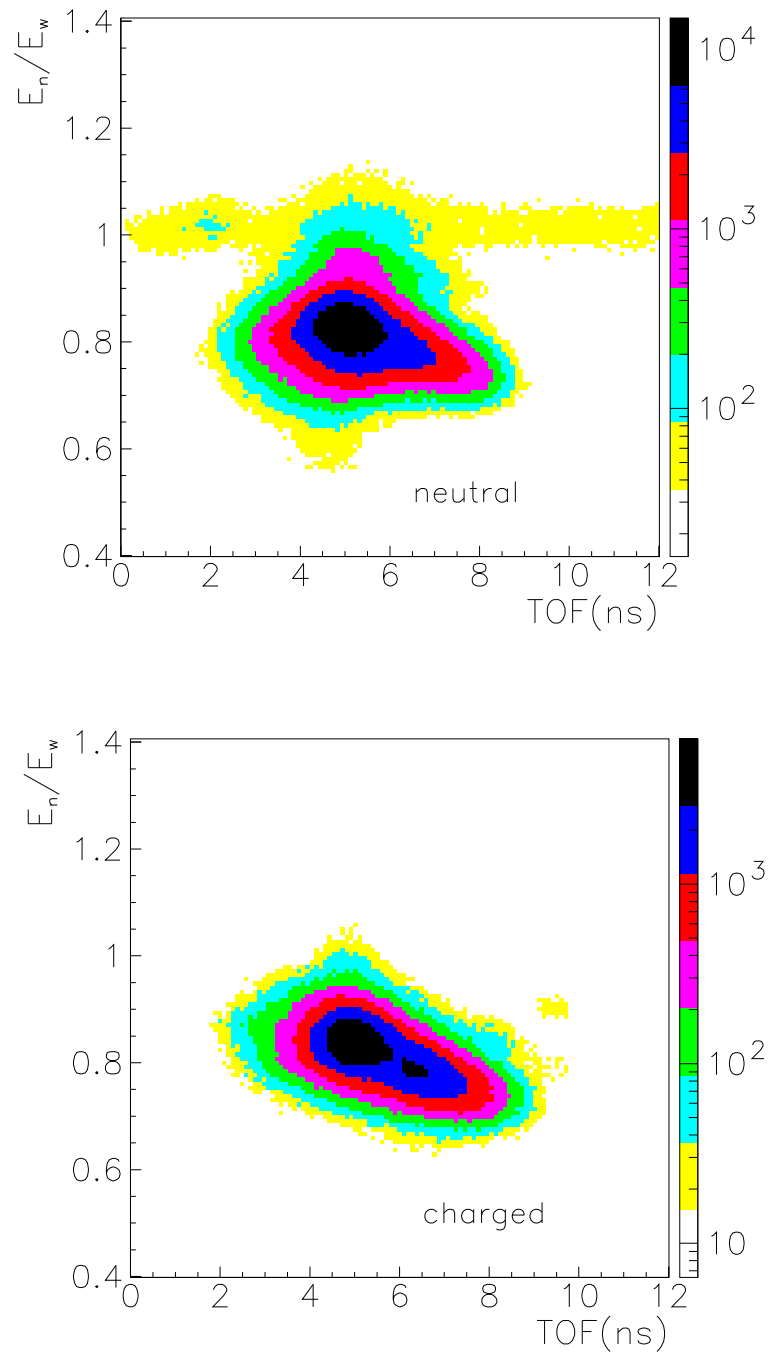
Figure 4.12: *Overall TAPS PSA versus TOF for particles with deposited energies of 60 MeV< E_w <100 MeV: a) neutral particles (no CPV hit) and b) charged particles (with CPV signal).*

As expected, photons are located in a region centered at 1.87 ns and PSA = 1. While hadronic particles are located in a wide region at lower PSA and higher TOF, except for the so-called "neutron low contour", with a PSA about 1, (see Fig.4.11). The neutron-low region corresponds to neutrons with energy far below 100 MeV, which mainly interact in the crystal via (n, γ) reactions and so, they exhibit an electromagnetic like PSA. Hence, these neutrons can only be discriminated from photons because of their higher TOF value. Taking benefit of the information (fired or not) delivered by the charged particle veto,
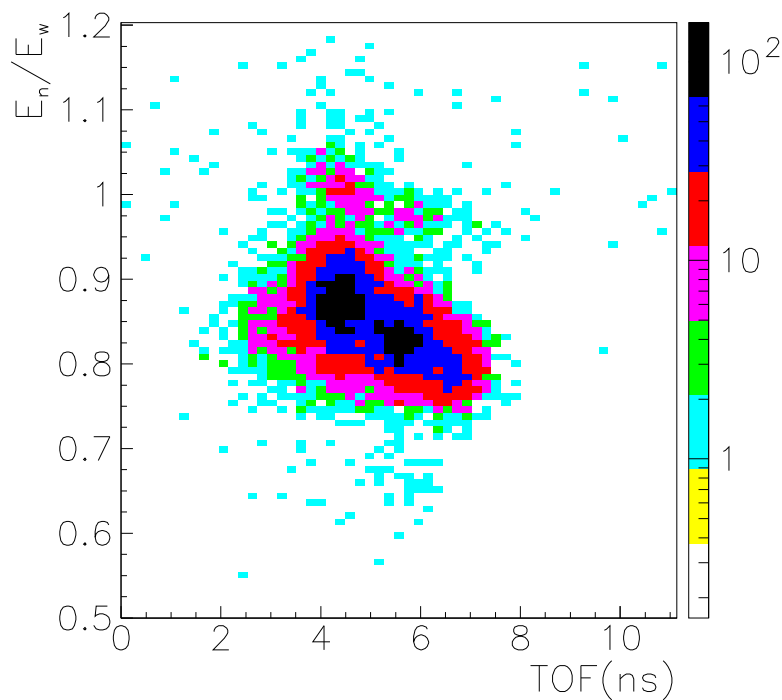

Figure 4.13: E_n/E_w vs TOF with an energy wide gate of $E_w > 100$ MeV. Inside the proton region two components can be distinguished: a first one with time-of-flight around 4 ns corresponding to protons and, at higher time ($TOF \sim 5.5$ ns) and lower PSA, to the deuteron region.

CPV, of each module, the PSA-TOF spectra of neutral and charged particles can be compared. From both panels of Figure 4.12 one can notice that the cosmic region is located at the neutral PSA-TOF spectra. The reason of this misidentification is that as cosmic muons have mainly vertical trajectories and thus they do not fire the CPV located at the front face of the BaF_2. Hence cosmic hits are tagged with a 0 CPV value.

Nevertheless, the cosmic background (which also contains the above-mentioned neutron background component), will be eliminated. The charged particle panel of Fig. 4.12 shows that there are almost no electrons within the prompt peak. Indeed, we only find these light particles, with its time-of-flight $\sim$ 1.87 ns, at the spectra with deposited energy lower than 20 MeV. Although in the experiment we do not take advantage of TAPS as a particle detector [58], the PSA versus time-of-flight analysis allows to identify the different charged particle species, as protons and deuterons of Fig. 4.13. Comparing the PSA matrices for different E_w gates (see e.g. from Fig.4.11 to Fig. 4.13) one can notice that with increasing energy the relative photon statistics decreases and the hadron contour shifts in the direction of the prompt photon peak. That emphasizes the necessity of using not only the PSA but also the correlation with the TOF values for a correct particle identification.

4.3.1 PSA-TOF monitoring

The monitoring of PSA-TOF plots can help us to detect possible time and energy calibration errors or strange runs (unknown beam stops, electronic detectors problems/changes...) that have been missed in the previous calibration and monitoring procedures. In our experiment, various PSA-TOF plots have been generated: global plots in statistics and adding all detectors, as well as per blocks, per individual detectors and dividing the statistics in sets of runs. Fig. 4.14 shows the PSA distributions for the E_w gate 20 MeV< E_w <60 MeV of 7 different run sets which cover all the experiment statistics. After performing this monitoring for all 5 E_w gates and solving different calibration problems, the fact that the positions of both (electromagnetic and hadronic) peaks remain constant confirms the validity of the energy calibration method. PSA-TOF projections in TOF for different energy gates between 10 and 100 MeV are plotted in Fig.4.15. As expected, the prompt peak intensity decreases strongly when increasing the energy. This behavior evinces the importance of having a high statistics data sample and also of a good photon discrimination method if we want to study the hard photon ($E_\gamma > 30$ MeV) production mechanism in such a hadron dominated environment.

4.4 Particle identification criteria

Once we have checked the response of BaF_2 detectors, a PID (Particle Identification) file is generated from the features observed in PSA-TOF plots. This file contains the
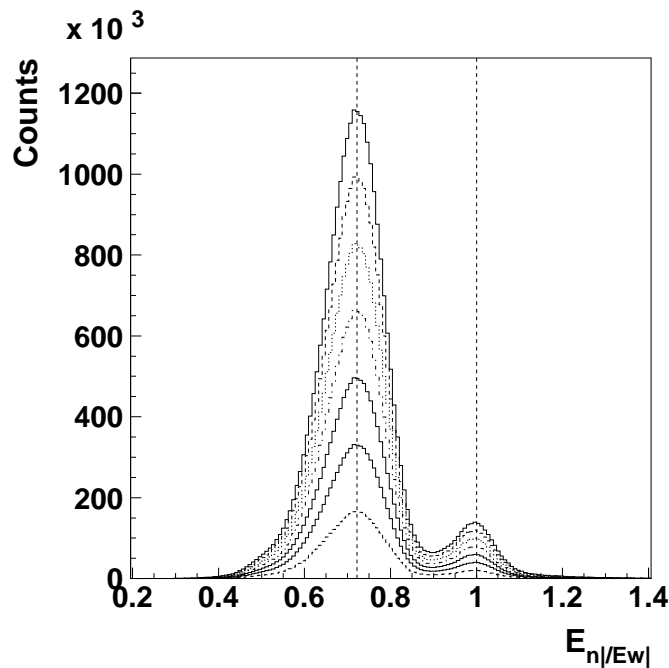
Figure 4.14: *Distribution of the PSA parameter of all the modules for 7 different run sets covering all the statistics. The spectrum has been obtained by adding all the modules and with a deposited energy gate of 20 MeV< E_w <60 MeV. A scaling factor between each set of runs has been applied in order to separate the curves.*

definition of the different particle selection contours (Table 4.1). Nevertheless, a selection based on only the PSA-TOF criteria is not sufficient for an unmistaken γ identification. As we have already mentioned in the last section, at the lowest energies we also need the VETO information to separate photons from electrons. Therefore, we get an almost complete PID by the combination of PSA+TOF+VETO information:

- Photons are identified as contour Gamma and no CPV hit;

- Electrons and positrons are identified as contour Gamma and CPV hit;

- Protons, high energy neutrons, deuterons, ..., are identified as contour Proton and CPV hit;

- High energy neutrons are identified as contour Proton and no CPV hit;

- Slow neutrons are identified as contour Neutron Low (PSA~ 1 and TOF> 5 ns) and no CPV hit;

- Cosmics Rays are identified as contour Cosmics (actually this contour is also composed of the environment neutron background) and no CPV hit.

Concerning the selection of the cosmic contour, we have seen at the PSA-TOF analysis that cosmic muons are mainly identified as neutral particles with random TOF. Therefore, cosmic muons within a TOF in the photon prompt peak will be identified as photons. However, as we will see in next section, this effect will be corrected defining for each photon energy range a cosmic contour far from the photon contour, but with the same TOF and PSA widths (see table 4.1).

4.5 Shower reconstruction

At this point we are at the border between dealing with TAPS raw data and dealing with physically meaningful data, since now each TAPS individual fired module has been

Particle contour	Energy wide	TOF	PSA
Gamma	(5 - 10) MeV	(0.00 - 4.80) ns	0.00 - 2.00
	(10 - 20) MeV	(0.00 - 4.16) ns	0.77 - 1.60
	(20 - 60) MeV	(0.00 - 3.54) ns	0.87 - 1.55
	(60 - 100) MeV	(0.00 - 2.77) ns	0.96 - 1.11
	> 100 MeV	(0.00 - 2.66) ns	0.97 - 1.10
Neutron	(0 - 100)	(5.36 - 19.65) ns	1.13 - 1.42
Proton	(5 - 10) MeV	(5.20 - 19.30) ns	0.26 - 1.89
	(10 - 20) MeV	(3.18 - 14.80) ns	0.35 - 0.89
	(20 - 60) MeV	(2.02 - 12.50) ns	0.36 - 0.90
	(60 - 100) MeV	(2.00 - 8.76) ns	0.56 - 0.94
	> 100 MeV	(2.00 -7.45) ns	0.73 - 1.11
Cosmics	(5 - 10) MeV	(32.00 - 36.80) ns	0.00 - 2.00
	(10 - 20) MeV	(32.00 - 36.16) ns	0.77 - 1.60
	(20 - 60) MeV	(32.00 - 35.54) ns	0.87 - 1.55
	(60 - 100) MeV	(32.00 - 34.77) ns	0.96 - 1.11
	> 100 MeV	(32.00 - 34.45) ns	0.97 - 1.10

Table 4.1: *Definition of the different particle selection rectangular contours used in the particle identification ROSEBUD routine.*

related to a type of particle. In the next analysis step, the response of fired modules induced by the same incident particle has to be correlated to identify electromagnetic showers initiated by photons.

When a photon with an energy of some MeV hits a BaF_2 module, it induces an electromagnetic cascade, producing $e^{\pm}$ and secondary photons, which will spread over a bunch of neighbor detectors, forming a *cluster*. The shower reconstruction will be performed by the second TAPS analysis software package, ROSEBUD, by means of its libraries and a cluster algorithm. The cluster algorithm needs information contained in 3 resource files: a file which contains the geometrical TAPS parameters, a TAPS neighbor modules file and the PID file generated from the PSA-TOF analysis.

First, the algorithm searches for clusters in each TAPS block; when it finds a detector which has fired it checks which direct neighbor modules have also fired, and selects them as clusters components, only if the energy deposited in each module is greater than 0.9 MeV. It continues the same task with second neighbors and next until the cluster is formed. The cluster will be identified as a shower only if the deposited energy in, at least, one detector of the cluster exceeds 10 MeV.

BaF_2 material is not only sensitive to photons but also to the rest of electromagnetic particles and hadrons. Therefore, the next task of the identification routine is to sort showers in two main groups: electromagnetic or hadronic depending on wether at least one module of the shower is of photon/electron type or not, respectively. Finally, once photons are identified as incident particles, their energies and incident positions will be computed. Some global parameters of the electromagnetic showers are calculated in order to recover the energy and direction of the impinging particle [79]. In short:

- The energy of the incident photon, E, is obtained adding the incident energies deposited in each cluster module, E_i:

$$E = \sum_i E_i \tag{4.4}$$

This energy, E, has still to be corrected in order to obtain the absolute calibration for photons.

- The photon direction, **r**, is obtained by means of the energy weighted sum over the vectors, **r**$_i$, pointing from the target to each cluster detector [80]:

$$\mathbf{r} = \frac{\sum_i W_i \mathbf{r_i}}{\sum_i W_i} \tag{4.5}$$

where:

$$W_i = MAX\{0, W_o + ln\frac{E_i}{E}\} \tag{4.6}$$

with the energy independent parameter $W_o = 4$, obtained from GEANT simulations. However, in this calculation, as we are involving $\mathbf{r}_i$, one assumes that the photon generates the shower just at the front face of the module. So, a correction [38] in $\mathbf{r}$ is introduced in order to take into account that actually, the photon creates the first electron pair after traversing , in average, a distance:

$$Z = MAX\{0, 1.2X_0 + ln\frac{E}{E_c}\} \tag{4.7}$$

where $E_c = 12.7$ MeV is the critical energy for BaF_2 and $X_0 = 2.05$ cm is its radiation length.

4.6   Photon energy correction factor

Once the FOSTER ntuple of each run was transformed into a ROOT tree by ROSEBUD, the produced trees were copied onto 22 "Data Summary Tapes" (DST), contained in 3490 cartridges.

Before constructing the photon spectra from the analysis of these DSTs, a *photon energy correction factor* is applied to take into account two independent effects. On the one hand, there is an appreciable amount of electromagnetic shower energy escaping at the front and back sides of the TAPS modules as well as from the modules at the borders of the blocks. This shower leakage introduces a shift in the reconstructed photon energy described by a factor f_l, which is calculated by means of GEANT [81] simulations to be in average 1.08. On the other hand, as mentioned in section 4.3, the difference in light production efficiency for muons and photons introduces another systematic shift in the photon energy which is corrected by a second factor f_s. Both factors are combined in a single factor as $f_E = f_l \cdot f_s$. Therefore, the corrected photon energy reads $E_\gamma(MeV) = f_E \cdot E(\text{MeV})$. In other TAPS experiments [82, 83, 73, 26] this global factor has been deduced from the comparison of the position of the mass peak of π^0 mesons (identified by an invariant mass analysis of the experimental $\gamma\gamma$ spectrum) and the true value $m_{\pi^0} = 134.9$ MeV. Since neutral pion production is marginal at a $50A$ MeV bombarding energy, in our experiment we have taken a $f_E = 1.15$, the average of the slightly different ($f_E = 1.11\text{-}1.18$) values deduced in the several TAPS experiments performed up to now. This energy correction factor introduces an estimated systematic error of 3%.

Therefore, we have considered a systematic error in the energy measurements of 6%, taking into account the uncertainty in the energy calibration method and the systematic error of the f_E factor.
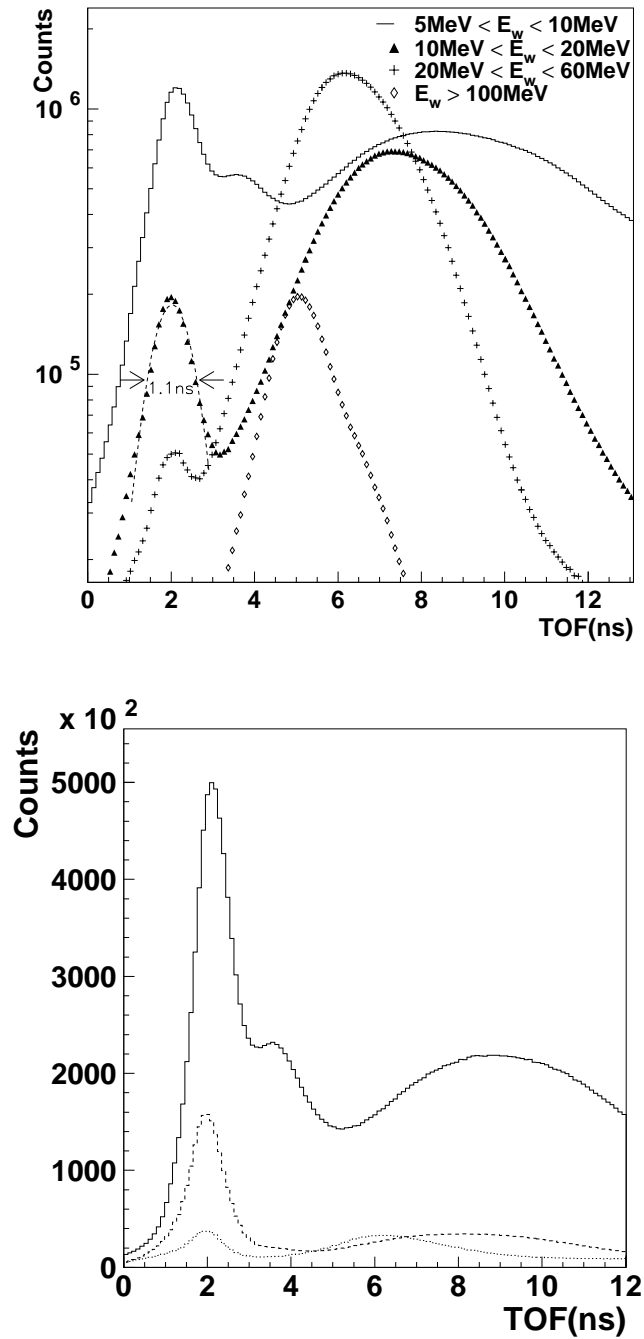
Figure 4.15: *a) TOF spectrum obtained by adding all the TAPS modules for different considered energy domains. b) TOF spectrum defined with the condition of 0.9< PSA <1.1 makes more apparent the photon peak, the three curves correspond to the energy domains of 10 MeV< E_w <20 MeV (solid line), 20 MeV< E_w <60 MeV (dashed line) and 60 MeV< E_w <100 MeV (dotted line).*

Chapter 5

Analysis of the charged particle multidetectors

The data analysis of the charged particle multidetectors is aimed at measuring the different charged particle multiplicities which, as we will see in chapter 7, will enable the selection of reaction classes of interest. In the next sections the inclusive event by event analysis of the Silicon Strip Detector, Dwarf Ball and Forward Wall is presented. First, I will briefly introduce the physical principle of the charge identification ΔE - E technique. This technique allows the charge identification of light charged particles and intermediate mass fragments detected in the DB and in the FW, and of the projectile like fragments and IMF impinging on the SSD. In sections 5.2, 5.3 and 5.4, the analysis carried out for each multidetector is described.

5.1 ΔE - E telescope identification technique

The charged particle identification technique for detectors composed of two stages or 2 materials, as the SSD or the DB and the FW, is based on the ΔE - E relation described by the Bethe-Bloch formula [84], which can be approximated by:

$$\frac{dE}{dx} \propto A \cdot Z^2 \, / \, E_{tot} \qquad (5.1)$$

where Z, and A are the charge and the mass of the incident particle. Measuring the energy lost in the first detector ΔE, by a charged product of kinetic energy E_{tot}, and the residual energy loss E $= E_{tot} \text{-} \Delta$E in the second detector, the product A$\cdot Z^2$, characteristic of a given isotope, can be determined. In practice, the $A \cdot Z^2$ dependence is evinced by series

of hyperbolas visible in a ΔE - E plot. Usually, due to the available resolution the lines of isotopes corresponding to the same element Z overlap, making only possible a charge identification. A recent work on charge identification in ΔE - E telescopes is reported in reference [85].

5.2   Particle identification in the Dwarf Ball

As we have seen in Chapter 3, for each charged particle capable to traverse one of the 64 Dwarf Ball detectors 4 different signals were recorded: the ΔE deposited in the thin plastic scintillator (E_{fast}), both CsI(Tl) components (E_{slow} and E_{tail}) and the total time signal. For each detector, the LCP isotopic identification was done exploiting the pulse shape properties of the CsI(Tl) light, while the IMF were identified from the $E_{fast} - E_{slow}$ arrays by using the ΔE - E technique. A preliminary step of the particle identification analysis, consisted in the selection of those hits that belong to the same reaction, discarding hence the pileup events. This was done by defining for each detector a time window containing the prompt peak. Once the physical meaningful data are selected the particle identification procedure is carried out.

5.2.1   Pulse shape analysis for the CsI(Tl) crystals

Due to the Cs(Tl) light characteristics (see 3.5.2), the ratio of the two Cs(Tl) luminescent components depends on the charge and mass of the incident particle. Thus, plotting E_{tail} versus E_{slow} we can identify the different lines corresponding to the hydrogen isotopes (p, t, d) and to the ^3He and α particles (see the example of Fig. 5.1). Due to the finite thickness of the Cs(Tl) crystal the most energetic light ions can escape from the crystal. This means that there exists a maximum amount of energy that can be lost in the crystal. This maximum, the so-called "*punchthrough*" point, is easily identified in the E_{tail} - E_{slow} plot because both CsI(Tl) components first increase and then at the punchthrough point they start decreasing, drawing a closed loop. The position of the punchthrough depends on the energy of each type of particle and on the size of the CsI(Tl) crystal. So, punchthrough points are used for energy calibration in experiments for which energy information is required.

Besides the LCP curves, there is a region of a few hits above the proton loop, which correspond to neutral particle hits. Below the α parabola, we find the region of intermediate-

mass fragments. A parabola discriminating this region of fragments is used as a complementary condition in the IMF identification presented in the next subsection.
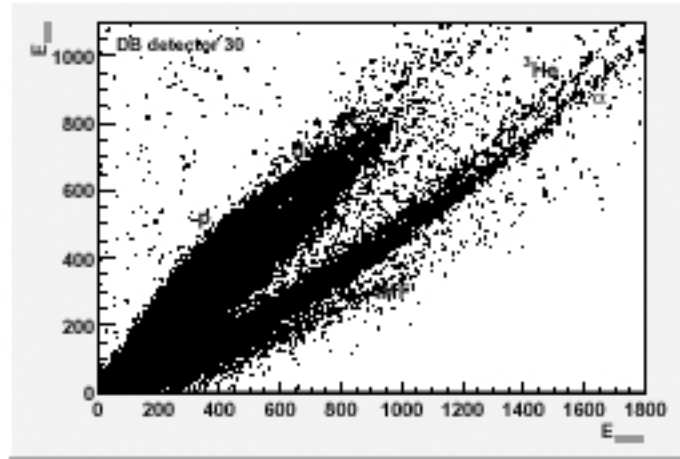

Figure 5.1: Example of bidimensional plot of both CsI(Tl) components, tail and slow, for particles detected in detector 30 of the Dwarf Ball. The lines of the hydrogen (p,d,t) and helium (^{3}He, α) isotopes are indicated.

5.2.2 ΔE-E analysis in the Plastic-CsI(Tl) phoswiches

In order to discriminate the charge of the intermediate-mass fragments we made use of the telescope geometry of each DB phoswich. Fig. 5.2 shows an example of E_{fast} versus E_{slow} bidimensional plot in which we identify different lines corresponding to the different charged particles for Z up to 9. However, in this second type of energy array an isotopic LCP identification can not be reached since the isotopes of hydrogen and the ^{3}He and α particles share the same wide regions. As a matter of fact, the energy resolution in the phoswiches ΔE-E spectra, as we will see below in the FW case, is not good enough to obtain an isotopic identification.

5.2.3 Particle identification method

The particle discrimination method is based on the definition of a function whose values depend only on the element and/or the isotope (A and Z) and not on the energy. Two identification functions were used for the isotopic LCP and the charge IMF identifications
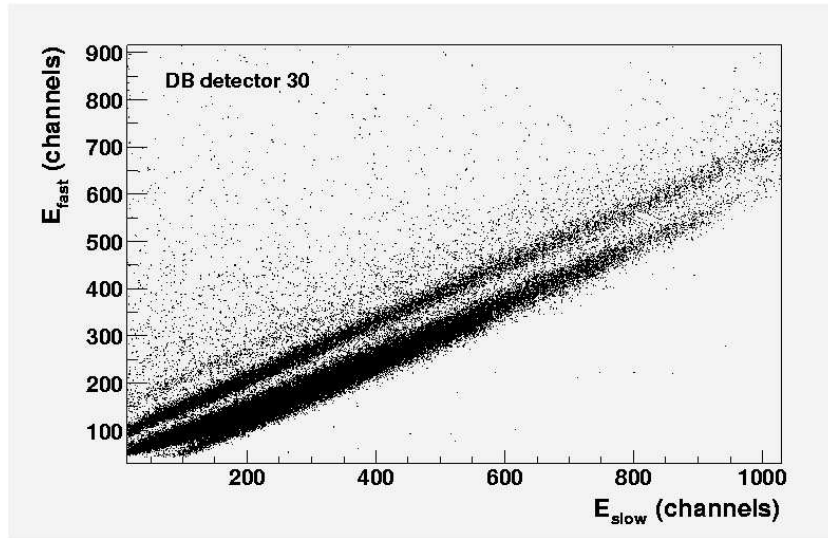
Figure 5.2: *E_{fast} versus E_{slow} histogram for the same detector as in Fig.5.1. Lines for Z up to 9 can be distinguished.*

in the DB, respectively:

$$P_{LCP} = \frac{E_{tail}}{(E_{slow} - C)} \tag{5.2}$$

$$P_{IMF} = (E_{fast} - A \cdot E_{slow}/B) \tag{5.3}$$

By analyzing the projection of the E_{tail} vs. E_{slow} and E_{fast} vs. E_{slow} spectra through the P_{LCP} and P_{IMF} parameters, the peak of each particle is identified. Fig. 5.3 shows an illustrative projection of a E_{fast} versus E_{slow} histogram through the P_{IMF} parameter for detector 22.

The time and noise thresholds and the values of the cuts of the two identification parameters for each one of the 64 DB phoswiches were stored in data files which were used in the subsequent analysis[1]. In the monitoring of the pulse shape spectra we detected different fluctuations of the particle lines, which were due to changes in the integration gates of the electronics during the performance of the experiment. Thus 5 different sets of identification parameters were used for 5 different groups of runs.

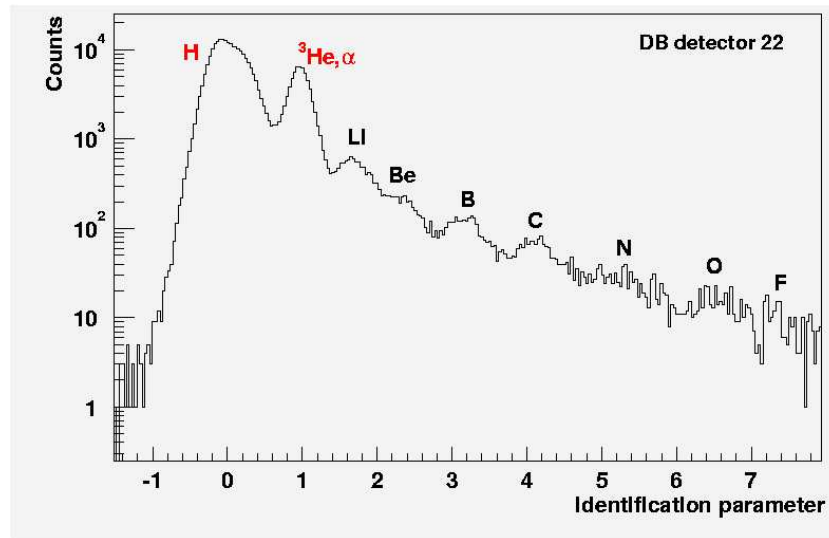[1]We followed the procedure described in more detail in [86].

Figure 5.3: *Example of projection of the bidimensional array E_{fast} versus E_{slow} for detector 22 using the P_{IMF} identification parameter. Each peak corresponds to a different element. Particles and fragments from H to F can be perfectly discriminated.*

5.3   Forward Wall analysis

The analysis technique carried out for the Forward Wall phoswich multidetector is very similar to the Dwarf Ball analysis. In the FW case, the traversing particle deposits a ΔE (E_{short}) in the thin NE102A plastic and it is stopped in the thick NE115, delivering the rest of its energy (E_{long}) or, if it is energetic enough, it punches through the phoswich. The time signal in the FW analysis is used, as in the DB case, to minimize background events by means of a cut of the time peak corresponding to prompt events.

As it can be seen in the illustrative plot of Fig. 5.4, different elements produce different banana shaped bands. The line of the form $E_{short} = C \cdot E_{long}$, located above the LCP and IMF curves corresponds to particles which are not energetic enough to arrive at the second plastic, and hence they cannot be identified.

The shape of the bands is found to be well described by a polynomial of third degree, and hence the defined identification parameter reads as:

$$P = (E_{short} - A \cdot E_{long} - B \cdot E_{long}^2 - C \cdot E_{long}^3)/D \qquad (5.4)$$

A representation of this particle identification function(E_{short}, E_{long}) for detector 6 is shown in Fig. 5.5. Whereas isotopes of hydrogen can be distinguished, the resolution
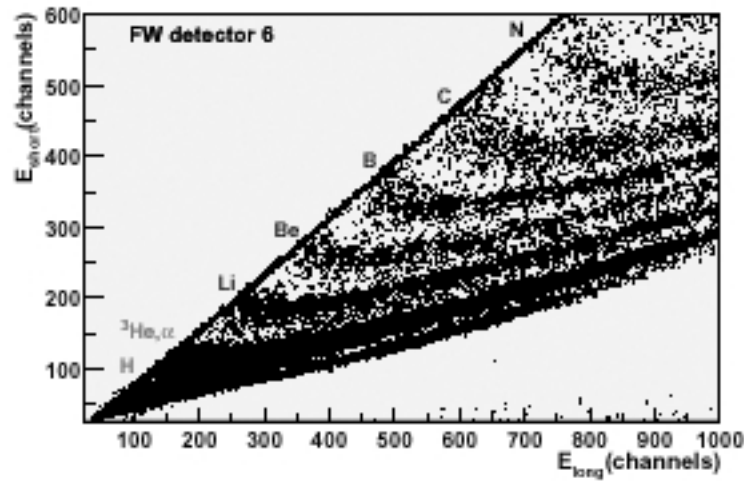
Figure 5.4: *Example of E_{short} versus E_{long} histogram for a FW plastic detector showing the bands corresponding to the different elements, from H to N.*
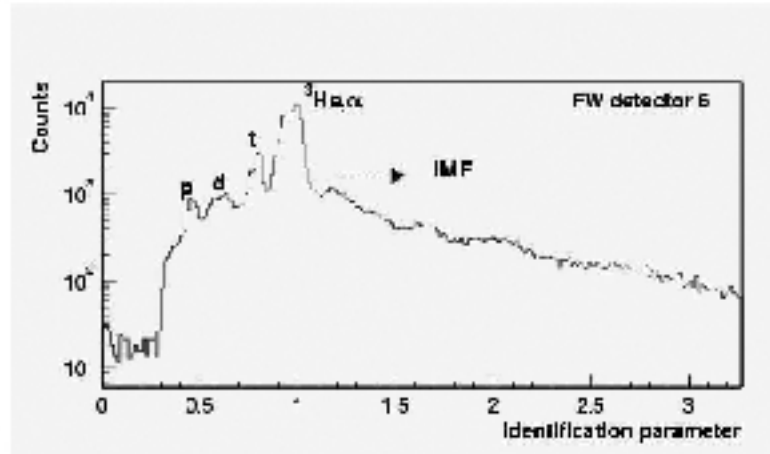

Figure 5.5: *Particle identification for the detector of Fig. 5.4 through the FW normalization function (E_{short}, E_{long}).*

of the FW does not enable the separation between ^{3}He and α particles and the peaks of the different fragments are not as well defined as in the DB case. Nonetheless, LCP

can be distinguished from IMF making a cut in the identification parameter between the He and Li peaks. That is the tool we have used to build the LCP and IMF multiplicity distributions which are presented in section 6.3.2.

In the case of the detectors positioned at the inner ring of the FW, the separation between the LCP and IMF could not be established, since the high counting rates at the inner ring made a clean particle discrimination impossible.

Unlike in the DB case, the identification parameters had to be changed only once during the analysis of the available statistics due to an only change in the particles curves positions.

5.4 Silicon Strip Detector analysis

5.4.1 ΔE - E spectrum

A charged particle hitting the SSD will deposit a ΔE in one of the 64 strips of the first and thin silicon strip disk and it will lose the rest of its energy E in one of the 128 strips of the subsequent and thicker disk. The fragment identification is done, as in the phoswich multidetectors, from the ΔE - E relation.

The ΔE vs. E histograms are plotted after superimposing the signals coming from the 64 circular strips and the 128 radial strips. To superimpose the signals the strips have been aligned i.e. relative calibrated. This calibration consists, first, in firing each one of the 192 strips by a pulser and taking the fired channel of one circular and of one radial strip as references. Then, a relative gain, with respect the reference circular (radial) strip, is defined for each radial (circular) strip. As in the case of TAPS, the Dwarf Ball and of the Forward Wall, a noise threshold or pedestal channel is defined for each individual SSD detector. But unlike in the Dwarf Ball and the Forward Wall, since no time signal is measured in the silicon strip telescope, a set of runs recorded off-beam is used instead in order to evaluate the background contribution. The aligned energy signal of a given strip i reads as:

$$E_i^{alig}(channels) = gain_i \cdot E_i^{raw}(channels) + pedestal_i \tag{5.5}$$

To identify each (ΔE,E) pair a condition in the SSD multiplicity has to be imposed to avoid the following situation. If two fragments hit simultaneously (in the same SSD subevent) the same SSD side (left or right) on the one side, the two fired circular strips

will provide the ΔE and the polar angle of each hit: $(\Delta E_1, \theta_1)$ and $(\Delta E_2, \theta_2)$. And the radial strips will measure the rest of the energy deposited in the SSD and the azimuthal directions of both incident particles: (E_1, ϕ_1) and (E_2, ϕ_2). Then, when reconstructing the hits by combining the radial and circular information 2 different cases are possible:

1. $(\Delta E_1, \theta_1, E_1, \phi_1)$ and $(\Delta E_2, \theta_2, E_2, \phi_2)$;

2. $(\Delta E_1, \theta_1, E_2, \phi_2)$ and $(\Delta E_2, \theta_2, E_1, \phi_1)$;

Due to this ambiguous reconstruction, one can not resolve the initial direction and the charge of each fragment. In consequence, events with a hit on more than one left or right circular and radial strip are rejected in the SSD analysis. Nevertheless, this condition does not reduce dramatically the SSD statistics, since most of the total (circular stage + radial stage) multiplicities are equal to 1 and 2, which correspond to one fragment stopped in the first or second stage, or that punches through the detector.

Fig. 5.6 shows an illustrative spectrum of circular energy (ΔE) versus radial energy (E) in the SSD. As in the case of the two phoswich multidetectors, reaction products of different charges form different hyperbolas. But since the SSD is not sensitive to light charged particles, the first line does not correspond to Z = 1. To identify the lines, the peak of the elastic diffusion is used [87].

The SSD has the drawback of being more delicate than the phoswich multidetectors exploited in our setup. On the one hand, the fast counting rates fasten the degradation of the silicon telescope and on the other, the positions of the pedestals are very sensitive to the SSD intrinsic noise. Unfortunately, in our experiment the resolution of the identification ΔE - E matrices worsen due to an increase of the intrinsic noise after the first recorded runs and hence, the charge identification per unit of elementary charge became impossible.

5.4.2   X - Y spectrum

The SSD fulfills a complete location of the fragments hitting both stages. Figure 5.7 shows the frontal view of the fired SSD. It can be noted that there are some "holes" accounting for several not working detectors, in this illustrative figure, 9 circular and 8 radial strips. The symmetry of the intensity of the particle hits with respect to the detector hole shows the good relative position of the beam and the SSD. Fig. 5.8 shows an example of the angular coverage of the SSD telescope.
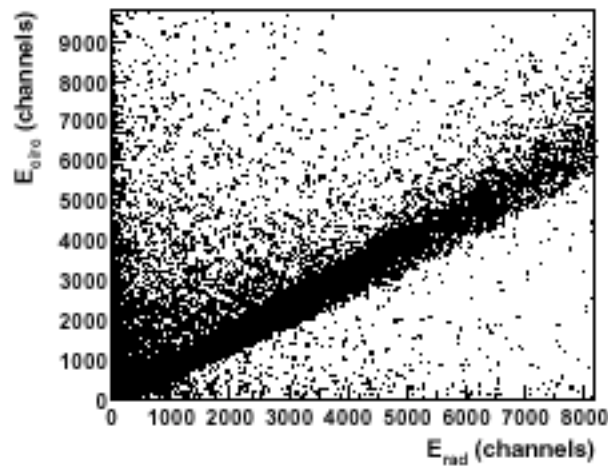
Figure 5.6: Example of Circular (E^{cir}) energy versus radial (E_i^{ra}) energy spectrum in the Silicon Strip Detector.
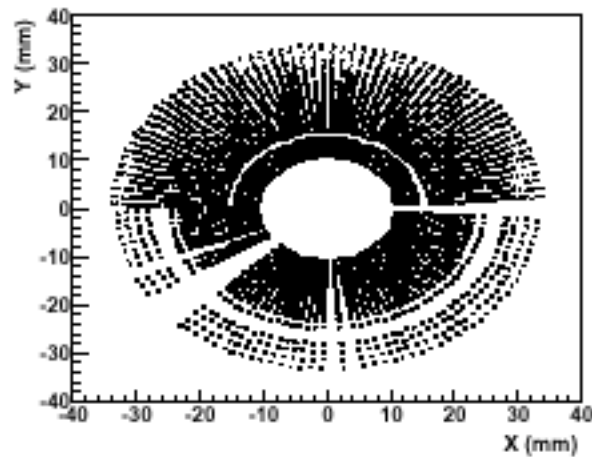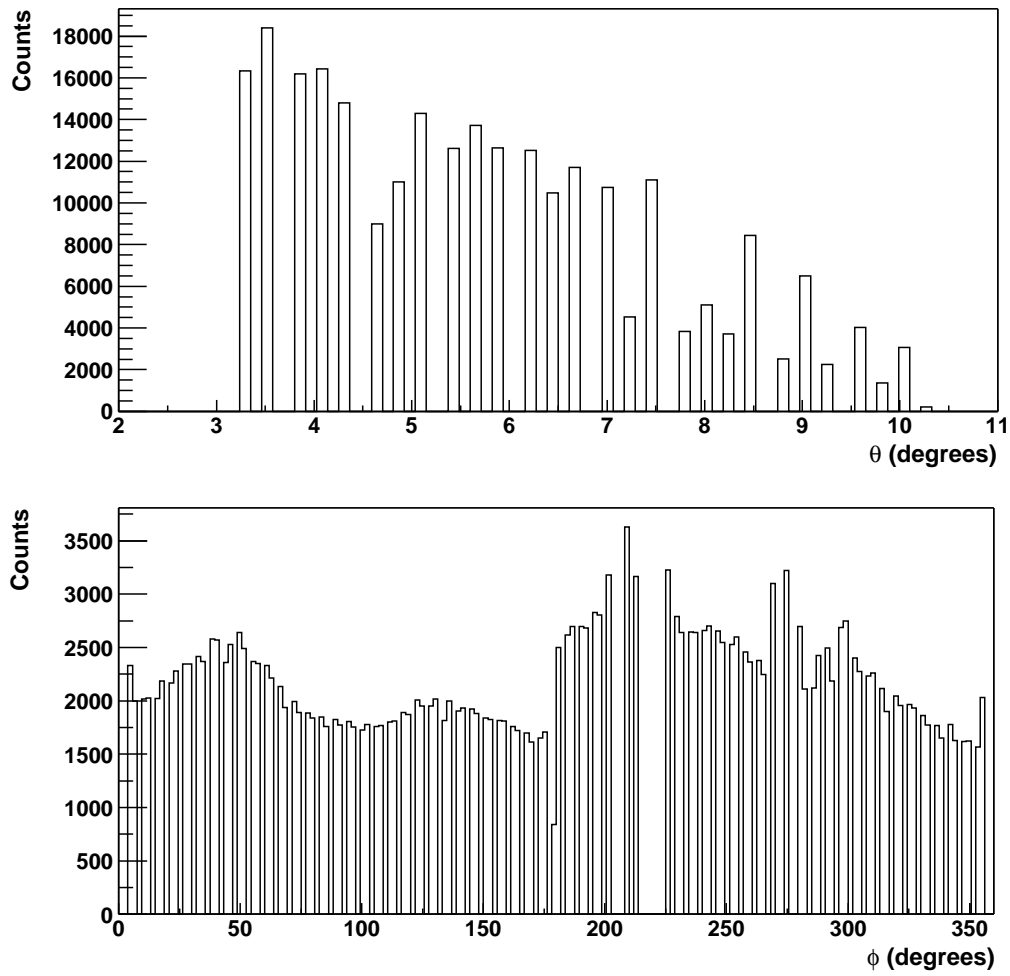

Figure 5.7: Frontal view of the first Silicon Strip Detector.

Figure 5.8: *Angular coverage of the fired SSD of Fig. 5.7.*